On the contributions of incipient vortex circulation and environmental moisture to tropical cyclone expansion

Jonathan Martinez[1], Chaehyeon Nam[1], and Michael Bell[1]

[1]Colorado State University

November 26, 2022

Abstract

This study investigates the contributions of incipient vortex circulation and mid-level moisture to tropical cyclone (TC) expansion within an idealized numerical modeling framework. We find that the incipient vortex circulation places the primary constraint on TC expansion. Increasing the mid-level moisture further promotes expansion but mostly expedites the intensification process. The expansion rate for initially large vortices exhibits a stronger response to increasing the mid-level moisture compared to initially small vortices. Previous studies have noted a proclivity for relatively small TCs to stay small and relatively large TCs to stay large; that is, TCs possess a sort of "memory" with respect to their incipient circulation. We reproduce this finding with an independent modeling framework and further demonstrate that an initially large vortex can expand more quickly than its relatively smaller counterpart; therefore, with all other factors contributing to expansion held constant, the contrast in size between the two vortices will increase with time. Varying the incipient vortex circulation is associated with subsequent variations in the amount and scale of outer-core convection. As the incipient vortex circulation decreases, outer-core convection is relatively scarce and characterized by small-scale, isolated convective elements. On the contrary, as the incipient vortex circulation increases, outer-core convection abounds and is characterized by relatively large rainbands and mesoscale convective systems. A combined increase in the amount and scale of outer-core convection permits an initially large vortex to converge a substantially larger amount of absolute angular momentum compared to its relatively smaller counterpart, resulting in distinct expansion rates.

On the contributions of incipient vortex circulation and environmental moisture to tropical cyclone expansion

Jonathan Martinez[1], Chaehyeon Chelsea Nam[1], Michael M. Bell[1]

[1]Department of Atmospheric Science, Colorado State University

Key Points:

- An initially large vortex can expand more quickly than its relatively smaller counterpart
- Outer-core convection exhibits a scale-dependent response to varying the incipient vortex circulation
- Increasing the environmental moisture promotes expansion but mostly expedites the intensification process

Corresponding author: Jonathan Martinez, `jon.martinez@colostate.edu`

Abstract

This study investigates the contributions of incipient vortex circulation and mid-level moisture to tropical cyclone (TC) expansion within an idealized numerical modeling framework. We find that the incipient vortex circulation places the primary constraint on TC expansion. Increasing the mid-level moisture further promotes expansion but mostly expedites the intensification process. The expansion rate for initially large vortices exhibits a stronger response to increasing the mid-level moisture compared to initially small vortices. Previous studies have noted a proclivity for relatively small TCs to stay small and relatively large TCs to stay large; that is, TCs possess a sort of "memory" with respect to their incipient circulation. We reproduce this finding with an independent modeling framework and further demonstrate that an initially large vortex can expand more quickly than its relatively smaller counterpart; therefore, with all other factors contributing to expansion held constant, the contrast in size between the two vortices will *increase* with time.

Varying the incipient vortex circulation is associated with subsequent variations in the amount and scale of outer-core convection. As the incipient vortex circulation decreases, outer-core convection is relatively scarce and characterized by small-scale, isolated convective elements. On the contrary, as the incipient vortex circulation increases, outer-core convection abounds and is characterized by relatively large rainbands and mesoscale convective systems. A combined increase in the amount and scale of outer-core convection permits an initially large vortex to converge a substantially larger amount of absolute angular momentum compared to its relatively smaller counterpart, resulting in distinct expansion rates.

Plain Language Summary

A variety of atmospheric and oceanic processes contribute to the expansion of a tropical cyclone wind field. We examine a subset of factors with idealized simulations to better understand how tropical cyclones expand. When both the initial size of a tropical cyclone and the environmental moisture are varied in accordance with observations, we find that the initial size of a tropical cyclone places the primary constraint on the expansion of a tropical cyclone wind field. We verify that tropical cyclones possess "memory" of their size when they first developed such that a small tropical cyclone stays small and a large tropical cyclone stays large. We further demonstrate that large tropical cy-

clones can expand more quickly than their relatively smaller counterparts. The amount of moisture in the atmosphere modulates the expansion of a tropical cyclone wind field. A relatively moist environment facilitates the development of convection and a concomitant increase of wind speeds that contributes to an expansion of the tropical cyclone wind field. Our findings motivate additional research investigating the variability of processes contributing to the initial size of a tropical cyclone amidst Earth's warming climate system.

1 Introduction

Accurately forecasting the lateral extent of a tropical cyclone (TC) wind field provides critical information to assess the potential scope of its wind, precipitation, and storm surge related hazards. Climatological studies have shown that TCs are characterized by an expansive range of scales (Merrill, 1984; Chavas & Emanuel, 2010; Chan & Chan, 2012; Knaff et al., 2014); however, the processes contributing to variable TC sizes are not fully understood. Complex multi-scale interactions occurring between a TC and its ambient environment underlie the difficulties associated with accurately forecasting the lateral expansion of a TC wind field. Several risk analyses have demonstrated the importance of considering TC size metrics in assessing the potential amount of losses associated with landfalling TCs (e.g., Czajkowski & Done, 2014; Zhai & Jiang, 2014; Klotzbach et al., 2020). Furthermore, recent studies have demonstrated that TC size distributions among various ocean basins will shift toward larger TCs amidst Earth's warming climate system (Knutson et al., 2015). As societal exposure to TC hazards continues to escalate among expanding coastal communities (Klotzbach et al., 2018), a thorough understanding of the processes contributing to the lateral expansion of TC wind fields is necessary to prevent fatalities and mitigate economic losses.

In proceeding, we note that several metrics of "size" exist in the literature, each describing to varying degrees the lateral extent of the TC circulation. Rather than elaborating the utility of each metric, we will note a few among the more common employed in the literature and refer the reader to a subset of references listed below: Radius of the outermost closed surface isobar (ROCI; Brand, 1972; Merrill, 1984; Kimball & Mulekar, 2004), radius of hurricane-force winds (64 kt; Hill & Lackmann, 2009), radius of damaging-force winds (50 kt; Kimball & Mulekar, 2004; Xu & Wang, 2010), and the equivalent radii of tropical storm-force and gale-force winds (34 kt; Chan & Chan, 2012; Kilroy & Smith, 2017). Operational forecasting agencies, such as the National Hurricane Center and the Joint Typhoon Warning Center, routinely produce wind radii forecasts for the radius of hurricane-force winds, damaging-force winds, and tropical storm-force winds (Knaff et al., 2017). Following Kilroy and Smith (2017), we define TC size as the maximum extent of the azimuthally averaged tangential velocity equal to the radius of gale-force winds (34 kt) 1 km above the ocean surface (henceforth, R_{gales}). Furthermore, we define TC expansion as the process whereby R_{gales} increases and conversely, contraction as the process whereby R_{gales} decreases.

The two tails of the global TC size distribution represent vastly different scales, demonstrating the potential for TCs to exhibit remarkable structural differences. Early studies provided evidence for weak typhoons with compact circulations, referred to as "midget" typhoons (Arakawa, 1952; Harr et al., 1996). On the same tail of the TC size distribution are intense TCs with compact circulations, referred to as "micro-hurricanes" (Hawkins & Rubsam, 1966) or "strong dwarfs" when depicted on an intensity–kinetic energy diagram (Musgrave et al., 2012). Exemplars of intense TCs with compact circulations include Hurricane Inez (1966; Hawkins & Rubsam, 1966; Hawkins & Imbembo, 1976) and Hurricane Patricia (2015; Rogers et al., 2017; Doyle et al., 2017; Martinez et al., 2019). The opposite tail of the TC size distribution is characterized by TCs such as Super Typhoon Tip (1979), which at its most intense stage possessed a maximum sustained wind speed of $\sim$85 m s^{-1} and a radius of gale-force winds exceeding 1100 km (Dunnavan & Diercks, 1980). Together, the foregoing examples allude to the weak relationship between TC intensity and size (Merrill, 1984; Weatherford & Gray, 1988; Carrasco et al., 2014). Such profound differences in TC size further emphasize the difficulties in forecasting potential hazards as a TC approaches land, necessitating a better understanding of expansion at various stages during a TC's life cycle.

Inter-basin comparisons have demonstrated that TCs in the western North Pacific basin, on average, tend to be the largest (Merrill, 1984; Knaff et al., 2014). Seasonal variations in TC size have been noted in the North Atlantic and western North Pacific basins, with average sizes exhibiting a relative minimum during mid-summer months and a relative maximum during the fall (Brand, 1972; Merrill, 1984; Liu & Chan, 2002; Kimball & Mulekar, 2004). Although basin and season alone do not necessarily provide physical information to describe TC size differences, inter-basin and seasonal variations in meso-synoptic scale precursor disturbances to cyclogenesis and environmental conditions, such as sea-surface temperatures and moisture, are certainly among the many factors underlying observed differences in TC size. For example, Knaff et al. (2014) concluded that small TCs are favored when vertical vorticity is supplied by the incipient vortex disturbance rather than the synoptic environment. Liu and Chan (2002) found that large TCs in the western North Pacific tend to be associated with a southwesterly surge of environmental flow into the vortex at 850 hPa resulting from cross-equatorial monsoonal flow, whereas small TCs tend to be embedded within easterly flow. Congruous with the foregoing discussion, variance in TC size can be partly attributed to the scale of an incipient vortex and the ambient large-scale environment throughout a TC's life cycle.

Idealized modeling studies have sought to elucidate the most relevant processes governing TC expansion. Hill and Lackmann (2009) demonstrated that environmental humidity is an important factor contributing to TC size. Increasing the environmental humidity promotes a greater amount of PV generated by radially outward propagating spiral rainbands. PV generated by the spiral rainbands is then subsumed by the inner-core PV tower, increasing its lateral extent and spinning up the outer-core cyclonic wind field through a balanced response. Xu and Wang (2010) demonstrated that increasing the RMW of incipient vortices results in larger outer-core surface fluxes that promote stronger diabatic heating within spiral rainbands. Stronger diabatic heating within spiral rainbands promotes more boundary layer vorticity convergence that spins up the outer-core circulation, which in turn increases the surface fluxes at increasingly larger radii. Xu and Wang (2010) also demonstrated that varying the RMW of incipient vortices has a larger influence on the final size of a TC compared to varying the environmental moisture. Chan and Chan (2014) demonstrated that TC size exhibits a dependency on both initial vortex size and planetary vorticity. They argued that when holding the vortex size constant, angular momentum fluxes imparted by the Coriolis torque increase when displacing the vortex further north whereas radial fluxes of relative angular momentum decrease as a result of increased inertial stability. These competing effects on angular momentum fluxes were shown to be minimized at 25 N such that there may exist an "optimal" latitude for TC expansion. Chan and Chan (2015) demonstrated that expansion rates are not sensitive to the initial vortex intensity, but rather the outer-core wind profile radially outward of the RMW. Increasing the outer-core tangential winds produces larger absolute angular momentum that can be subsequently converged toward the TC center, thereby promoting larger expansion rates. Kilroy and Smith (2017) emphasized the importance of boundary layer dynamics in governing both the radial location of low-level ascent out of the boundary layer and the associated thermodynamic properties of this air. They demonstrated with the aid of a slab boundary layer model that an initially large vortex concentrates relatively weak ascent over a broad radial region near the axis of rotation compared to an initially small vortex that concentrates relatively strong ascent closer to the axis of rotation. The organization of ascent occurs prior to the development of deep convection. A larger vortex will therefore develop a broader distribution of diabatic heating and stronger inflow at larger radii, which in the presence of a larger radial absolute angular momentum gradient contributes to a more rapid spin-up of the outer-core circulation. A reasonable conclusion drawn from idealized modeling studies in aggregate is that TC expansion is inextricably linked to convectively driven convergence of absolute angular momentum toward the TC center of circulation.

The foregoing discussion demonstrates there are several internal and external factors contributing to TC expansion; however, our understanding of how these factors evolve together and contribute to TC expansion remains limited. In nature, “internal” and “external” factors are not entirely independent, precluding definitive statements regarding the relative contributions of one factor in one category over the other. Furthermore, employing a combined framework that integrates both internal and external factors is challenging and requires selecting from the numerous potential factors contributing to TC expansion in each respective category. Therefore, it is practical to limit the number of factors we explore and to investigate the underlying processes contributing to TC expansion associated with this reduced set of factors. Here we choose to examine the contributions of incipient vortex circulation and environmental moisture to TC expansion; that is, one “internal” and one “external” factor, respectively. Our choice is motivated by the aforementioned relevance of the incipient vortex circulation and environmental moisture when considering TC expansion.

Several past studies have noted a proclivity for relatively small TCs to stay small and relatively large TCs to stay large (e.g., Merrill, 1984; Knaff et al., 2014; Kilroy & Smith, 2017; Tao et al., 2020). The results presented herein reproduce this finding and indicate potential for additional, new insights regarding TC expansion. The following section discusses the methods to create variable incipient vortex circulations and environmental moisture profiles within the idealized numerical modeling framework. Section 3 presents results gathered from the simulations. Section 4 discusses the processes underlying TC expansion along with concluding remarks and avenues for future work.

2 Methods

2.1 Incipient Vortex Circulation

Previous studies investigating the contributions of initial vortex size to TC expansion within an idealized modeling framework begin by prescribing an axisymmetric vortex profile with a fixed tangential velocity maximum. A subset of vortices with different sizes is created by either varying the radius of maximum tangential winds (RMW; e.g., Xu & Wang, 2010; Kilroy & Smith, 2017; Xu & Wang, 2018) or fixing the RMW and varying the radial vortex shape outward of the RMW (e.g., Chan & Chan, 2014, 2015; Xu & Wang, 2018). Although the two methods vary a different element of the incipient vortex circulation, and thus likely differ in producing variable TC expansion rates, both methods more generally vary the incipient vortex circulation strength. That is, either increasing the RMW or decreasing the radial decay of tangential velocity outward of the RMW is tantamount to increasing the incipient vortex circulation strength.

We choose to fix the initial tangential velocity maximum and RMW while varying the radial decay of tangential velocity outward of the RMW to produce a set of incipient vortices. The radial structure of tangential velocity is prescribed via a modified Rankine vortex of the form

$$v(r) = \begin{cases} v_{max}\left(\frac{r}{r_{max}}\right) & 0 \leq r < r_{max} \\ v_{max}\left(\frac{r}{r_{max}}\right)^{-\alpha} & r \geq r_{max}, \end{cases} \tag{1}$$

where $v_{max} = 15$ m s^{-1} is the maximum tangential velocity, $r_{max} = 50$ km is the RMW, and α is the decay parameter. After the radial structure of the incipient vortices is prescribed, we apply a radial decay function following Nolan (2007) to ensure that the total circulation is zero in the doubly periodic model domain for 3-D simulations. The radial decay function is given by

$$v(r) = v_0(r)\exp\left(-\frac{r}{R}\right), \tag{2}$$

where $v_0(r)$ denotes the initial modified Rankine vortex profile given by (1), r is the radius, and R is chosen as 600 km. Figure 1 shows the tangential velocity and vorticity profiles after applying the radial decay function. Then, a linear vertical decay function is applied that reduces the tangential velocity to zero at an altitude of 20 km. Values of α are chosen as 0.3, 0.5, and 0.7, in accordance with observations of North Atlantic basin TCs (Mallen et al., 2005). It is unlikely that a tropical storm is characterized by as steep a radial decay of tangential velocity given by the $\alpha = 0.7$ vortex, but we examine this subset of vortices to elucidate the contributions of incipient vortex circulation to TC expansion. The $\alpha = 0.7$ and $\alpha = 0.3$ vortices will henceforth be referred to as small and large, respectively.

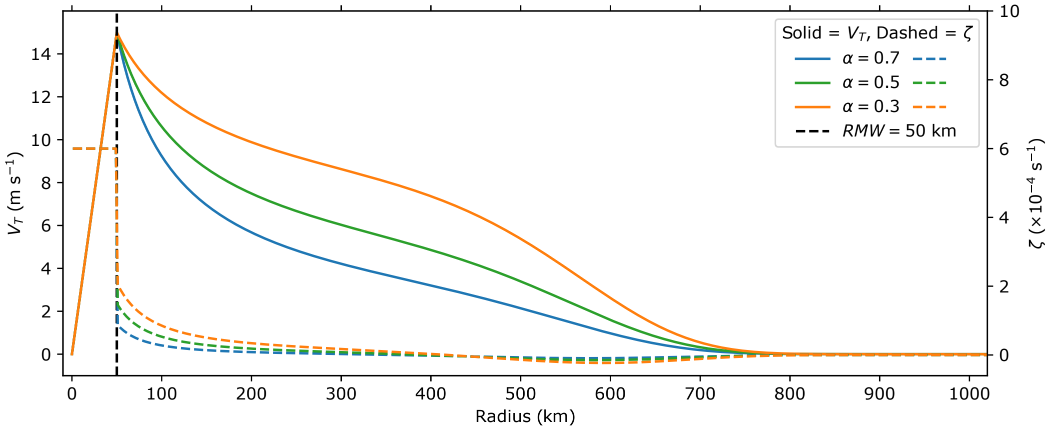

Figure 1. Axisymmetric radial profiles of tangential velocity (solid) and vertical vorticity (dashed) are shown for each of the incipient vortices. The decay parameter used for each modified Rankine vortex is given in the legend by α. A radial decay function (2) is applied to each of the tangential velocity profiles to ensure that the circulation is zero at the doubly-periodic boundaries of 3-D simulations. See section 2.3 for additional details.

2.2 Environmental Moisture

The degree to which environmental moisture modulates TC expansion will largely depend on its horizontal and vertical variations throughout the atmosphere. Prior studies investigating the contributions of environmental moisture to TC expansion often designate a sounding representative of the tropics, fix the temperature profile, and vary the mixing ratio; this method preserves the temperature while varying the relative humidity. For example, Hill and Lackmann (2009) placed their vortices in a moist envelope where the environmental humidity was held constant within 100 km of the incipient vortex center, linearly reduced between 100–150 km, and constant beyond 150-km radius. The environmental moisture reduction factor was applied uniformly in the vertical (i.e., no variations in the vertical were introduced beyond those given in the original sounding). Xu and Wang (2010) also applied a uniform reduction factor in the vertical to create variable initial environments. We adopt a methodology that is motivated by climatological studies demonstrating that tropical moisture variance is maximized near the mid-troposphere (e.g., Holloway & Neelin, 2009; Dunion, 2011). Furthermore, relatively high mid-tropospheric moisture content within tropical waves has been shown to be an important factor contributing to cyclogenesis (Davis & Ahijevych, 2013; Komaromi, 2013).

Beginning with the Dunion moist-tropical sounding (Dunion, 2011), we fix the temperature profile and systematically vary the vertical structure of moisture to produce a set of three soundings. The Dunion moist-tropical sounding is first interpolated to 40-

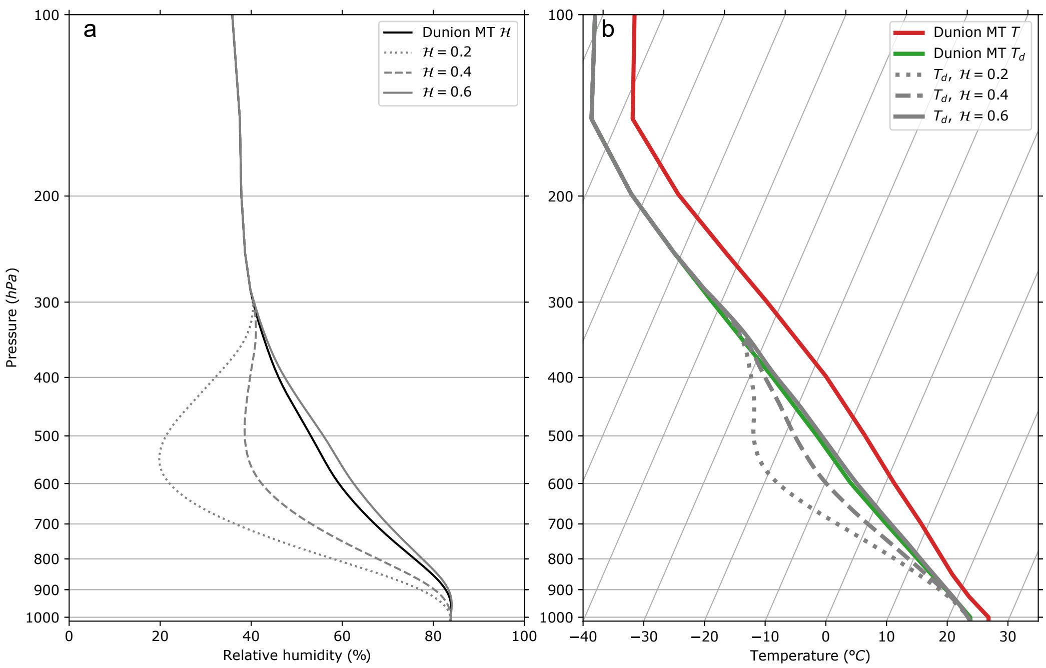

Figure 2. (a) Relative humidity ($\mathcal{H}$) is shown as a function of log-pressure for the Dunion moist-tropical sounding (black) and each of the environmental moisture profiles (gray). (b) Temperature and dewpoint temperature are shown as a function of log-pressure for the Dunion moist-tropical sounding (red and green, respectively), along with dewpoint temperature for each of the environmental moisture profiles (gray).

m vertical intervals between the surface and 10-km altitude. This region is smoothed using a 3-km low-pass Lanczos filter with 35 weights. Variations to the smoothed moisture profile are then introduced by applying a Hanning window with a multiplicative factor such that the relative humidity ($\mathcal{H}$) is set to 20%, 40%, or 60% at 4960-m altitude (∼560 hPa; Fig. 2a). The dewpoint temperature profiles are reconstructed with these variations and shown on a skew-t log-p diagram in Fig. 2b, along with the original Dunion moist-tropical sounding for reference. The $\mathcal{H} = 60\%$ sounding is nearly identical to the Dunion moist-tropical sounding, and the $\mathcal{H} = 20\%$ sounding resembles the mid-level moisture content observed during a Saharan air layer event in the North Atlantic basin (Dunion, 2011). We neglect initial horizontal moisture variations aside from those required to satisfy thermal wind balance when superposing an axisymmetric vortex circulation onto a horizontally homogeneous environment. This method is limited in its representation of nature where TCs often develop in asymmetric distributions of moisture; however, we find it fruitful to examine the expansion of TCs in a simplified framework that can be generalized to represent a larger set of environments in future work. The $\mathcal{H} = 20\%$ and $\mathcal{H} = 60\%$ environments will henceforth be referred to as dry and moist, respectively.

2.3 Numerical Model Setup

Numerical simulations are carried out with the non-hydrostatic, fully compressible Cloud Model 1 (CM1) version 19.7 (G. H. Bryan & Fritsch, 2002). As described above, the incipient vortex circulation and environmental moisture are varied to create three different initial conditions for each parameter, resulting in nine experiments. Each of the nine experiments are simulated with the axisymmetric configuration of CM1, and the four experiments representing the small/large incipient vortices and the dry/moist environments are simulated with the full, three-dimensional configuration of CM1. Axisymmetric simulations are computationally inexpensive, and therefore an ensemble of ten axisymmetric simulations is produced for each of the nine experiments in the original set. The 3-D experimental design is chosen to aid in delineating the underlying processes contributing to TC expansion in three dimensions by selecting the extrema of initial conditions. Following V. S. Nguyen et al. (2008), we introduce random moisture perturbations with an amplitude of $\pm$ 0.5 g kg^{-1} to the lowest 500 m of the axisymmetric simulation domains. This method is chosen to examine the sensitivity of TC expansion, and the processes discussed herein, to stochastic processes such as deep, moist convection.

The axisymmetric grid spans 3050 km in radius and is defined with a uniform 1-km radial grid spacing in the innermost 300 km that gradually stretches to 10-km spacing at the domain boundary. There are 800 radial grid points in total. The vertical grid spans 28 km in altitude and is defined with a grid spacing that stretches from 50- to 500-m in the lowest 5.5 km and is a uniform 500-m above 5.5 km. There are 65 vertical grid points in total, with 12 lying in the lowest 2-km altitude. A Rayleigh damping layer is applied 100 km from the outer horizontal boundary and above 22-km altitude to aid in mitigating the reflection of internal gravity waves.

The 3-D grid spans 2040×2040 km in the horizontal and is defined with a uniform 2.5-km grid spacing in the innermost 1200 km that gradually stretches to 11.5-km spacing at the domain boundaries. There are 600×600 horizontal grid points in total. The vertical grid and Rayleigh damping layer applied above 22-km altitude are identical to those used in the axisymmetric simulations. We note that the radial grid spacing in the axisymmetric domain is not identical to the horizontal grid spacing in the 3-D domain. The principal findings in this study are not sensitive to the choice of axisymmetric grid spacing (not shown), and therefore we opt to present results from the axisymmetric simulations with a finer 1-km radial grid spacing.

Rather than placing the 3-D vortices in a quiescent environment, we gradually impose a 5 m s^{-1} uniform westerly flow throughout the domain following a methodology similar to the time-varying point-downscaling (TVPDS) technique (Onderlinde & Nolan, 2017). The uniform flow is introduced by adding a Newtonian relaxation term to the horizontal momentum equations, given by

$$\frac{\partial u}{\partial t} = \ldots - \frac{\langle u \rangle - u_{ref}}{\tau_n}, \tag{3}$$

and

$$\frac{\partial v}{\partial t} = \ldots - \frac{\langle v \rangle - v_{ref}}{\tau_n}, \tag{4}$$

where $\langle u \rangle(z)$ and $\langle v \rangle(z)$ denote the domain-averaged zonal and meridional wind velocities, respectively, $u_{ref}(z,t)$ and $v_{ref}(z,t)$ denote the reference zonal and meridional wind profiles to nudge toward, respectively, and τ_n is the nudging time scale. Thus, domain-averaged winds at each vertical level are nudged toward a specified reference profile that is a function of height and time, avoiding the introduction of a net circulation into the domain. The nudging time scale τ_n controls the rate at which the domain-averaged winds are nudged toward the reference wind profile. We permit each of the vortices to develop deep, moist convection for 24 h prior to introducing the 5 m s^{-1} uniform westery flow with a 6-h nudging time scale. A time-varying translational domain is updated each hour in the simulation to track the minimum of a smoothed pressure field that represents the approximate center of each vortex, and the domain translation velocity vector is subtracted from the total wind to produce grid-relative winds. We further refine our specification of the center location with a 2–8 km layer-averaged pressure centroid following the method described by L. T. Nguyen et al. (2014).

All simulations are integrated for eight days on an f-plane corresponding to $\sim$16 °N latitude with underlying sea-surface temperatures fixed at 29 °C. Radiative processes are approximated via a simple 2 K day^{-1} Newtonian relaxation to the base-state temperature profile (Rotunno & Emanuel, 1987). Microphysical processes are parameterized using the Morrison double-moment scheme with graupel selected as the large ice category (G. H. Bryan & Morrison, 2012). Sub-grid-scale turbulent processes are parameterized using a first-order local closure, commonly referred to as the "Louis PBL scheme" (Louis, 1979; Kepert, 2012; H. G. Bryan et al., 2017). The horizontal and vertical eddy viscosities are separately determined given the local flow deformation and the moist Brunt-Väisälä frequency. The heat diffusivity is taken as identical to the momentum diffusivity such that the Prandtl number is unity. This turbulence parameterization requires specifying the horizontal and vertical mixing length scales, chosen herein as $l_h = 1000$ m and $l_v = 100$ m, respectively for both the axisymmetric and 3-D simulations.

3 Results

3.1 Intensity and Initiation of Rapid Intensification

The intensity of each simulated TC is shown as a function of time in Fig. 3, where intensity is approximated as the maximum azimuthally averaged wind speed at the lowest model level (25 m). There are no discernible intensity relationships as a function of either incipient vortex circulation or environmental moisture for the axisymmetric ensemble averages, whereas an initially larger incipient vortex circulation and larger environmental moisture produce slightly higher-intensity TCs for the 3-D simulations. Discrepancies in the timing to begin rapid intensification (RI) are noted among the axisymmetric ensemble averages and the 3-D simulations. Consistent with previous studies, larger tropospheric moisture content expedites the development phase and initiation of RI as the incipient vortex is more quickly moistened, thereby promoting deep convection (e.g., Tao & Zhang, 2014; Kilroy & Smith, 2017). We define the initiation of RI following a method similar to that used by Judt and Chen (2016) and Rios-Berrios et al. (2018), which is motivated by the approximate 95th percentile of 24-h over-water TC intensification rates in the North Atlantic basin (Kaplan et al., 2010). The initiation of RI is specified as the first (hourly) time step where the subsequent 24-h intensification rate exceeds 15.4 m s^{-1} and each of the 6-h intensification rates within the 24-h time window exceeds 3.8 m s^{-1}. Black dots in Fig. 3 denote the initiation of RI for each simulation following this definition. To account for timing discrepancies in the initiation of RI and provide a more consistent comparison of TC evolution, we subtract off the time when RI begins from each simulation unless otherwise specified. Furthermore, to facilitate the discussion of results as a function of incipient vortex circulation and environmental moisture, we abbreviate references to each simulation as follows: small (S), large (L), dry (D), and moist (M). For example, the simulation with a decay parameter of $\alpha = 0.7$ and mid-level environmental moisture of $\mathcal{H} = 20\%$ is referred to as the SD simulation.

3.2 RMW and R_{gales} Evolution

Time series of the azimuthally averaged RMW at the lowest model level and R_{gales} are shown for all simulations in Fig. 4. In each of the axisymmetric ensemble averages, the RMW contracts to approximately 10-km radius during the intensification phase and subsequently expands for the remainder of the simulation. 3-D simulations illustrate a similar contraction of the RMW during intensification; however, the RMW does not expand subsequent to the intensification phase for the small TCs. Both sets of axisymmetric and 3-D simulations show that for a given environmental moisture, as the incipient vortex circulation increases, the resulting RMW is larger at all times during the TC life cycle. Furthermore, the axisymmetric ensemble averages show that for a given incipient vortex circulation, TCs embedded in environments with larger moisture content attain a larger RMW; however, this relationship is not present for small TCs in the 3-D simulations.

Figure 4 elucidates the principal finding of this study; the incipient vortex circulation places the primary constraint on TC expansion, and in part establishes the expansion rate. An initially large vortex ($\alpha = 0.3$) expands more quickly than its rela-

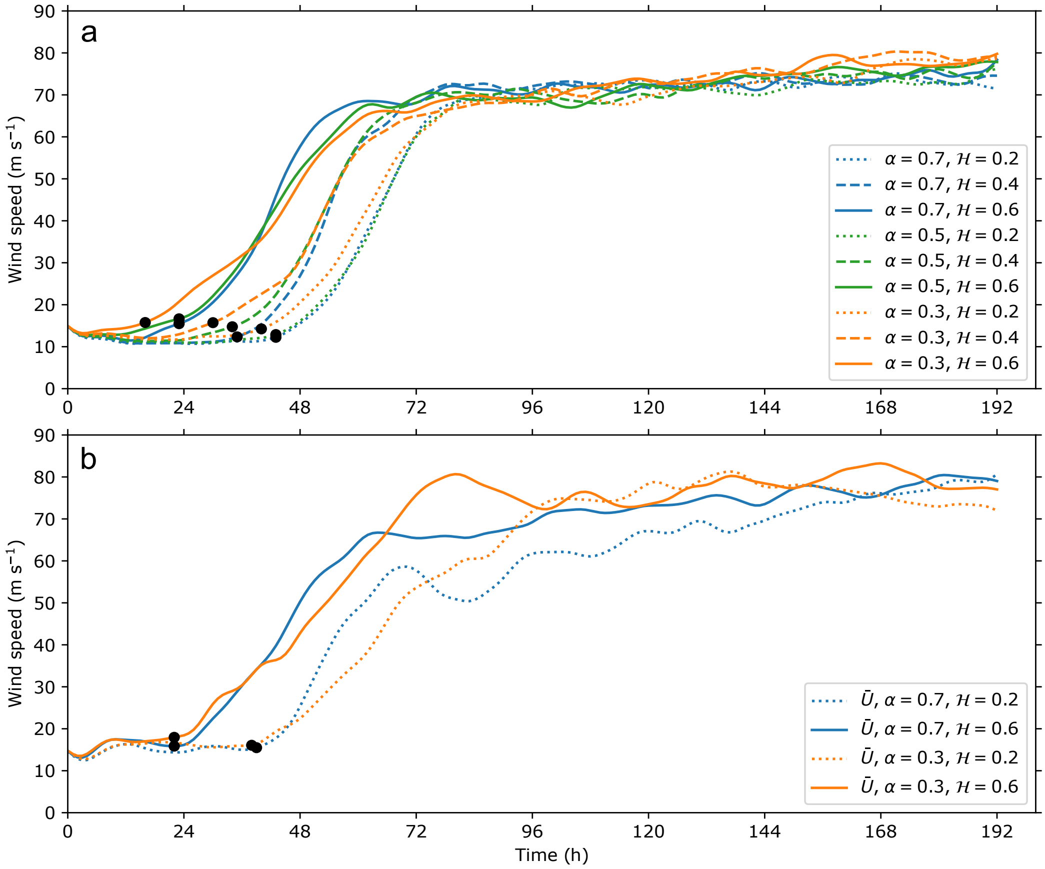

Figure 3. The maximum azimuthally averaged wind speed at the lowest model level (25 m) is shown as a function of time for (a) the nine axisymmetric ensemble averages (10 ensemble members each) and (b) the four 3-D simulations. Simulations are distinguished by the modified Rankine vortex decay parameter (α, color) and by the mid-level environmental relative humidity ($\mathcal{H}$, line style). $\bar{U}$ denotes the presence of a uniform 5 m s^{-1} westerly flow for 3-D simulations (see section 2.3 for details). Black dots denote the initiation of rapid intensification for each respective simulation. Each time series is smoothed using a 12-h low-pass Lanczos filter with nine weights.

tively smaller counterpart ($\alpha = 0.7$); therefore, with all other factors contributing to expansion held constant, the contrast in size between the two vortices *increases* with time. Increasing the environmental moisture produces larger TCs when the timing to rapid intensification is left unaccounted; however, a more consistent comparison accounting for the timing to RI reveals that the expansion rate is only slightly modulated by increasing the environmental moisture. The axisymmetric ensemble averages show a slightly larger expansion rate as the environmental moisture is increased for a given incipient vortex circulation. The degree to which varying the environmental moisture modulates the expansion rate in the 3-D simulations is dependent on the incipient vortex circulation. Increasing the environmental moisture does not influence the expansion rate for initially small vortices, whereas increasing the environmental moisture results in larger expansion rates for initially large vortices. Furthermore, Figs. 4c,d show that as the RMW begins to expand for the large 3-D vortices, the expansion rate increases. Henceforth, results will only be discussed for the 3-D simulations.

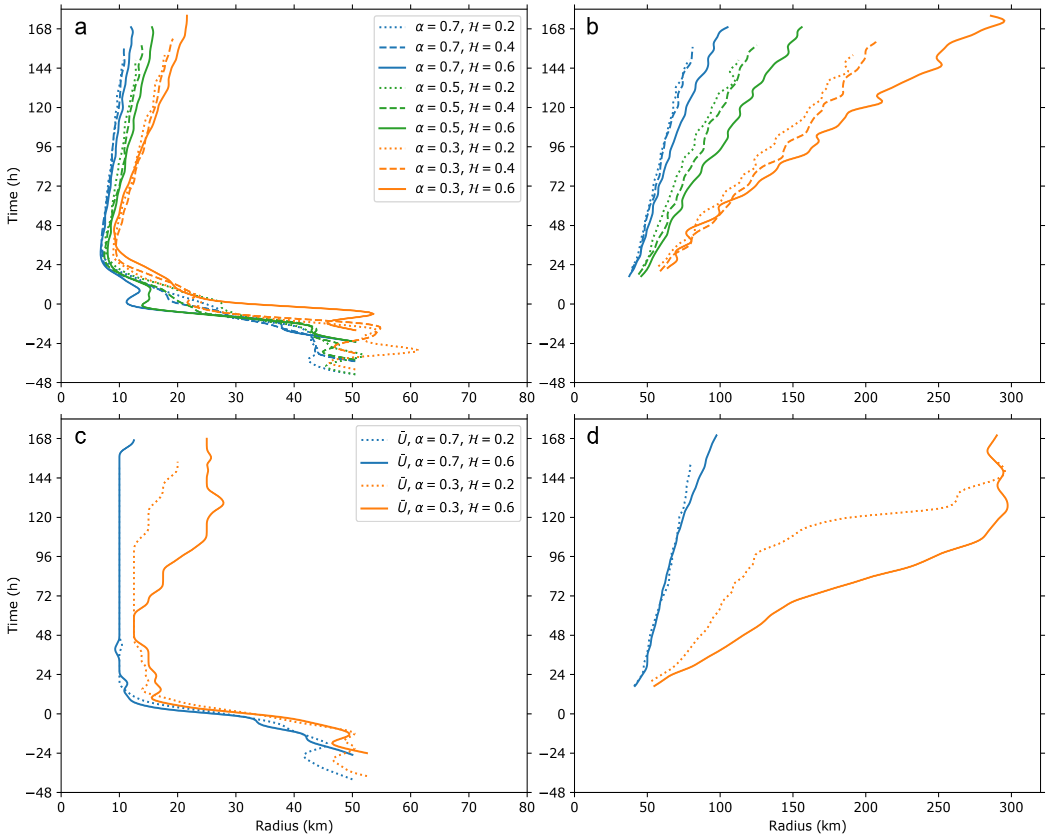

Figure 4. The radius of maximum tangential winds (RMW) and the radius of gale force winds (R_{gales}) are shown as a function of time with respect to the initiation of rapid intensification for (a,b) the nine axisymmetric ensemeble averages and (c,d) the four 3-D simulations, respectively. Simulations are distinguished by the modified Rankine vortex decay parameter (α, color) and mid-level environmental relative humidity ($\mathcal{H}$, line style). $\bar{U}$ denotes the presence of a uniform 5 m s^{-1} westerly flow for 3-D simulations (see section 2.3 for details). Each time series is smoothed using a 12-h low-pass Lanczos filter with nine weights.

As noted in section 1, TC expansion is inextricably linked to convectively driven convergence of absolute angular momentum toward the TC center of circulation. To illustrate this relationship, Fig. 5 shows the azimuthally averaged evolution of absolute angular momentum (M) for each TC at 1-km altitude. Overlaid in orange is the M surface corresponding to $3.0{\times}10^6$ m^2 s^{-1} (for simplicity, the $M = 3.0$ surface) for each respective TC. The large TCs begin with larger outer-core M compared to the small TCs and subsequently converge a substantially larger amount throughout their life cycles. Furthermore, the extent of radial inflow is a function of incipient vortex circulation, such that the small TCs do not have radial inflow exceeding 3 m s^{-1} beyond 100-km radius. Collectively, this evolution is captured by the $M = 3.0$ surface beginning at approximately 300-km radius for the small TCs and contracting ∼50–75 km, whereas the $M = 3.0$ surface begins at approximately 230-km radius for the large TCs and contracts over 200 km; the $M = 3.0$ surface is eventually subsumed into the inner-core circulation of the LM TC (Fig. 5d). A combination of initially larger outer-core M and a broader extent of radial inflow contributes to the large TCs converging a substantially larger amount of M throughout their life cycles compared to the small TCs. The following sections will demonstrate that this finding is primarily related to the areal distribution and nature of convection found in the outer-core region.

3.3 Convective Evolution

The evolution of convection for each 3-D simulation is shown by azimuthally averaged radar reflectivity (dBZ) in Fig. 6. Each simulated TC is characterized by vigorous eyewall convection near the RMW, denoted by reflectivity values exceeding 50 dBZ. Notable differences are found radially outward of the RMW, where decreasing the incipient vortex circulation strength or environmental moisture generally corresponds to less convection. Figures 6c,d show that the aforementioned expanding RMW in the large TCs is accompanied by radially propagating convection that contributes to an expansion of the eyewall in both simulations. We examined animations of radar reflectivity and potential vorticity (PV) and noted an increase in the amount of spiral rainband convection and a subsequent growth of the eye region during the time period that the RMW expands for the large TCs (not shown). The animations suggest that the eyewall may have expanded via PV mixing near the eye–eyewall interface or an eyewall replacement

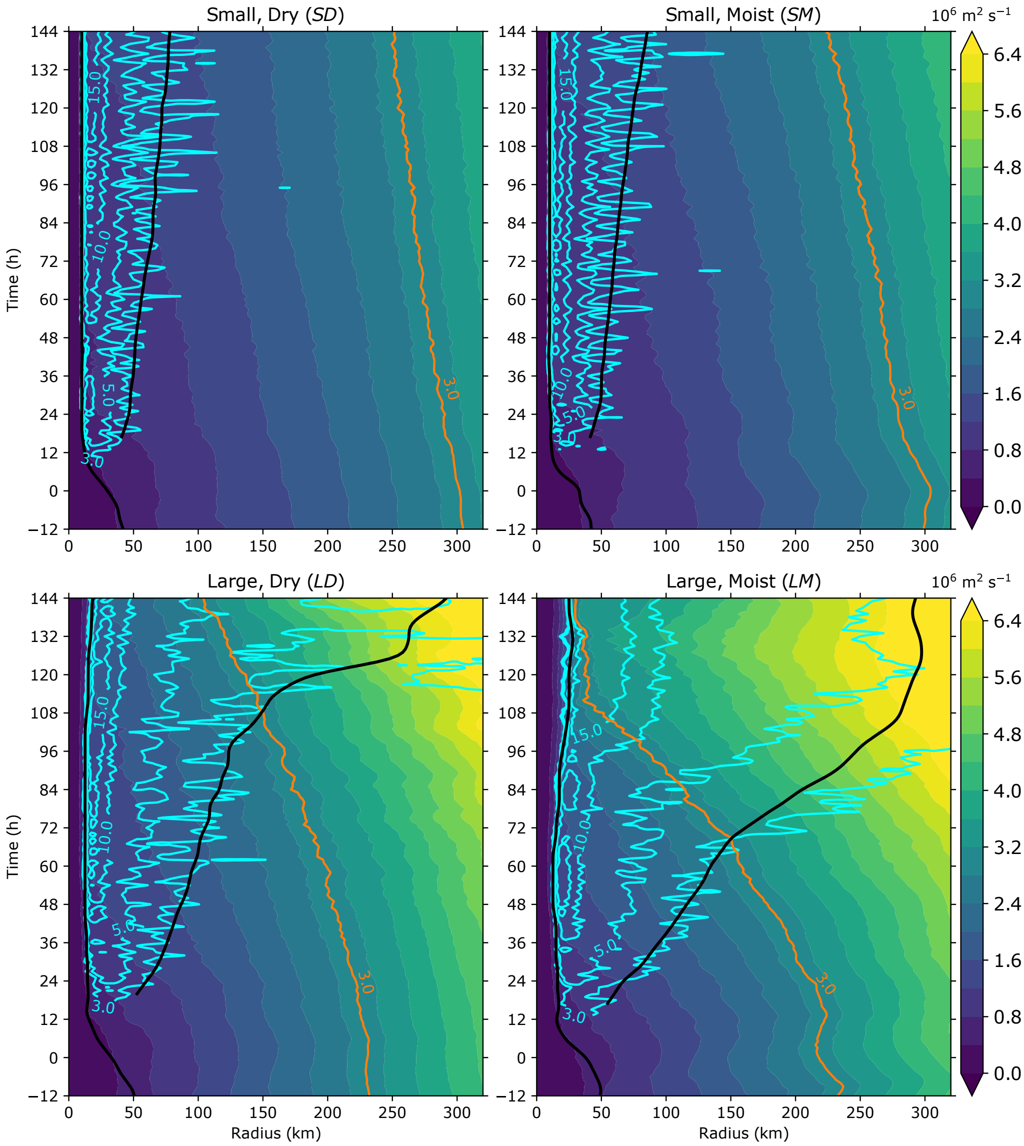

Figure 5. Azimuthally averaged absolute angular momentum at 1-km altitude (shaded), 0–1 km altitude layer-averaged radial inflow magnitude (cyan contours at 3, 5, 10, and 15 m s^{-1}), and the absolute angular momentum surface corresponding to 3.0$\times$10^6 m^2 s^{-1} (orange) are shown as a function of time relative to the initiation of rapid intensification for the 3-D simulations: (a) *SD*, (b) *SM*, (c) *LD*, and (d) *LM*. The innermost black curve in each panel is the radius of maximum tangential winds (RMW) and the outermost black curve is the radius of gale-force winds (R_{gales}).

cycle. We reserve a thorough analysis of the processes contributing to eyewall expansion in the large TCs for future work.

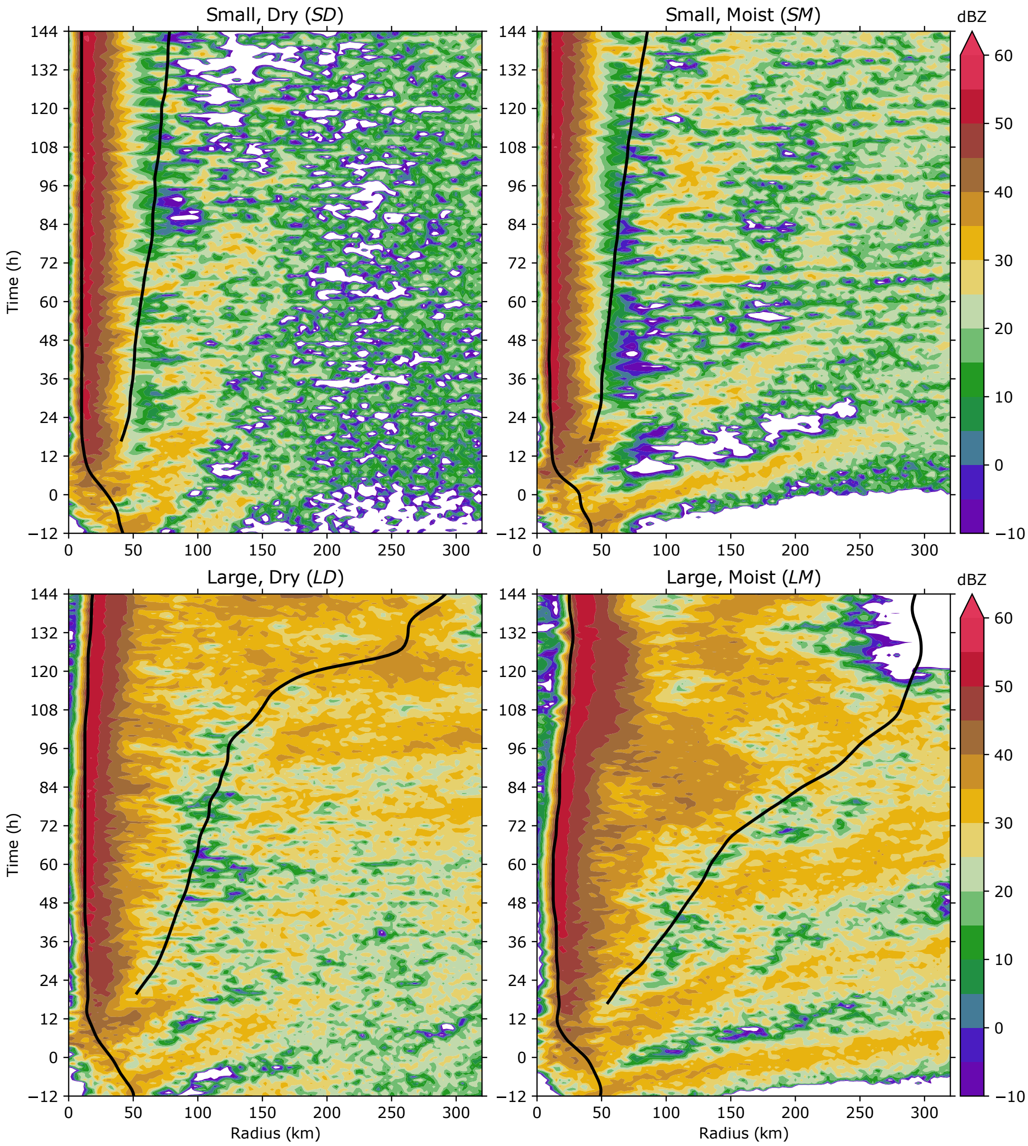

Figure 6. Radar reflectivity (dBZ) at 2-km altitude is shown as a function of radius and time relative to the initiation of rapid intensification for the 3-D simulations: (a) SD, (b) SM, (c) LD, and (d) LM. The innermost black curve in each panel is the radius of maximum tangential winds (RMW) and the outermost black curve is the radius of gale-force winds (R_{gales}).

Cartesian snapshots of radar reflectivity at 2-km altitude, 72 h after the initiation of RI, are shown for each simulation in Fig. 7. As the incipient vortex circulation is decreased, outer-core convection is relatively scarce and characterized by small-scale, isolated convective elements. On the contrary, as the incipient vortex circulation is increased, outer-core convection abounds and is characterized by relatively large-scale rainbands and mesoscale convective systems. Varying the environmental moisture slightly increases the areal coverage of convection, but does not appear to have a significant influence on the spatial scale of outer-core convection.

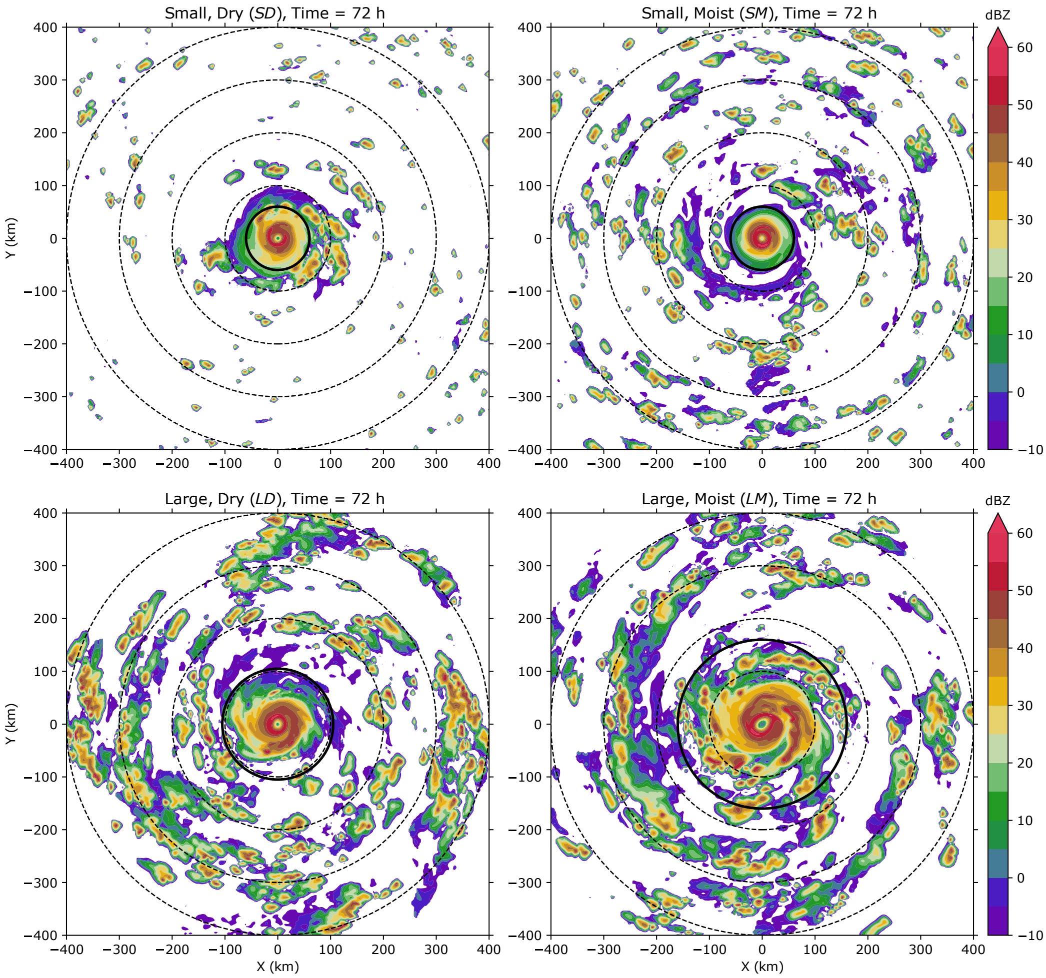

Figure 7. Cartesian snapshots of radar reflectivity (dBZ) at 2-km altitude, 72 h after the initiation of rapid intensification, are shown for the (a) SD, (b) SM, (c) LD, and (d) LM simulations. Radius rings in increments of 100 km from the center of each TC are given by the dashed-black lines and the radius of gale-force winds (R_{gales}) for each respective TC is given by the solid black line.

The relationship between incipient vortex circulation and the scale of outer-core convection is quantified by representing the reflectivity at 2-km altitude, given by $Z(r, j, t)$, as a Fourier series along the azimuthal dimension

$$Z_m(r,t) = \sum_{j=0}^{J-1} Z(r,j,t)\left[cos(2\pi mj/J) + isin(2\pi mj/J)\right], \tag{5}$$

where m is the azimuthal wavenumber ($m = 0, 1, 2, \ldots, 180$), r the radius, j the azimuth angle in degrees ($j = 0, 1, 2, \ldots, J = 360$), and t the time. The Fourier coefficient for each azimuthal wavenumber is given by $Z_m(r,t)$. Then, the power spectrum for each azimuthal wavenumber is given by

$$\mathcal{Z}_m(r,t) = \frac{1}{J^2}|Z_m(r,t)|^2, \tag{6}$$

and the normalized power spectrum for each azimuthal wavenumber is given by

$$\hat{\mathcal{Z}}_m(r,t) = \frac{\mathcal{Z}_m(r,t)}{\sum_m \mathcal{Z}_m(r,t)}. \tag{7}$$

The normalized power spectrum (7) is computed for reflectivity at 2-km altitude between 100–300 km radius and for each hourly time step. Normalized power spectra are then area-averaged between 100–300 km radius and cumulatively summed over all wavenumbers for each hourly time step.

Figure 8 shows the cumulative normalized power spectra at 48 h and 72 h after the initiation of RI for each simulation. The median cumulative power of outer-core reflectivity occurs between azimuthal wavenumbers 4–8 for the large TCs and above azimuthal wavenumber 9 for the small TCs. Therefore, the median distribution of convection is shifted toward larger scales as the incipient vortex circulation is increased. In general, the large TCs have a propensity to develop relatively large-scale convection in the outer-core region throughout their life cycle, regardless of environmental moisture. The outer-core convection for the small TCs exhibits a slightly greater scale-dependence on environmental moisture compared to the large TCs, with the moist environment producing larger scales of convection; however, Fig. 4d suggests that differences in the scales of convection between the SD and SM TCs have a negligible influence on the their expansion rates. This may be partly due to the longevity of convection that develops in the outer-core region or the relative scarcity of outer-core convection for the SD TC. The following section will further investigate differences in the nature of convection among the simulated TCs to elucidate the differences in expansion rates.

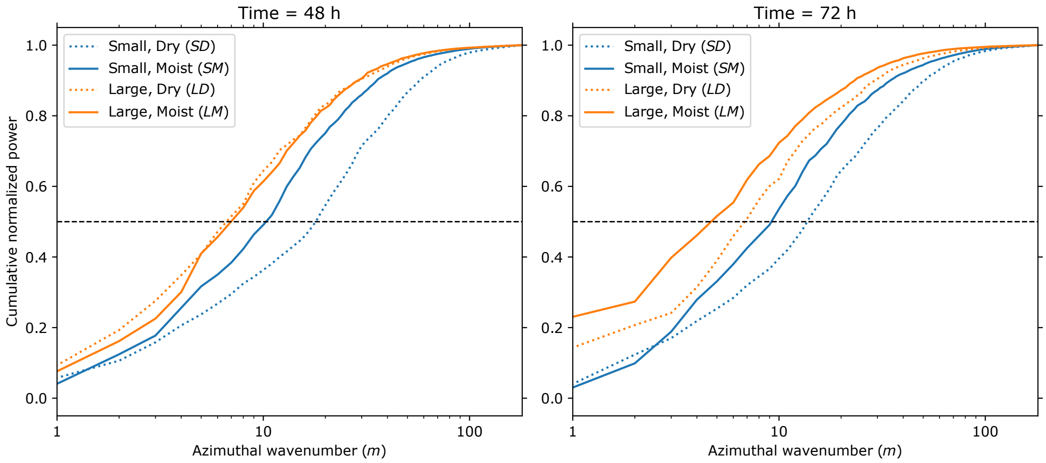

Figure 8. Cumulative normalized power spectra of outer-core (r = 100–300 km) radar reflectivity at 2-km altitude are shown as a function of azimuthal wavenumber (m) for each simulation at (left) 48 h and (right) 72 h after the initiation of rapid intensification. The dashed-black line denotes the median cumulative normalized power. See text for additional details on how the cumulative normalized power spectra are constructed.

3.4 Vertical Mass Flux Distributions

We begin comparing the nature of convection between the simulated TCs via frequency distributions of vertical mass flux within the inner- and outer-core regions. We define the inner-core region as the area enclosed by $r \leq 50$ km; this definition is chosen to capture the evolution of convection confined by the initial RMW for each TC (r = 50 km), including the eyewall, principal, and secondary rainbands (Houze, 2010). We define the outer-core region as the area enclosed by $100 \leq r \leq 300$ km; this definition is chosen to capture the evolution of convection beyond twice the initial RMW for each TC, including principal and secondary rainbands that propagate from the inner- to outer-core region and distant rainbands (Houze, 2010). We tested several definitions for the inner- and outer-core regions, including dynamic boundaries that follow the RMW (e.g., Hence & Houze, 2012). We elect to use the aforementioned static boundaries when distinguishing between the inner- and outer-core regions to preserve the same number of grid points compared between each TC and to avoid issues with boundaries that account for the RMW given that it flares radially outward at upper levels in the TC circulation. Results remain qualitatively similar when using a definition that accounts for the RMW. Furthermore, we created inner- and outer-core vertical mass flux frequency distributions as a function of altitude for various time windows and found that the results remain largely consistent regardless of the initial window time or length (not shown). Therefore, we choose to show the vertical mass flux frequency distributions during the 12-h time window beginning 48-h after the initiation of RI for each TC. This time window captures the evolution of convection in each TC subsequent to its bulk intensification phase (see Fig. 3) and coincides with the previous reflectivity spectral analysis (Fig. 8a).

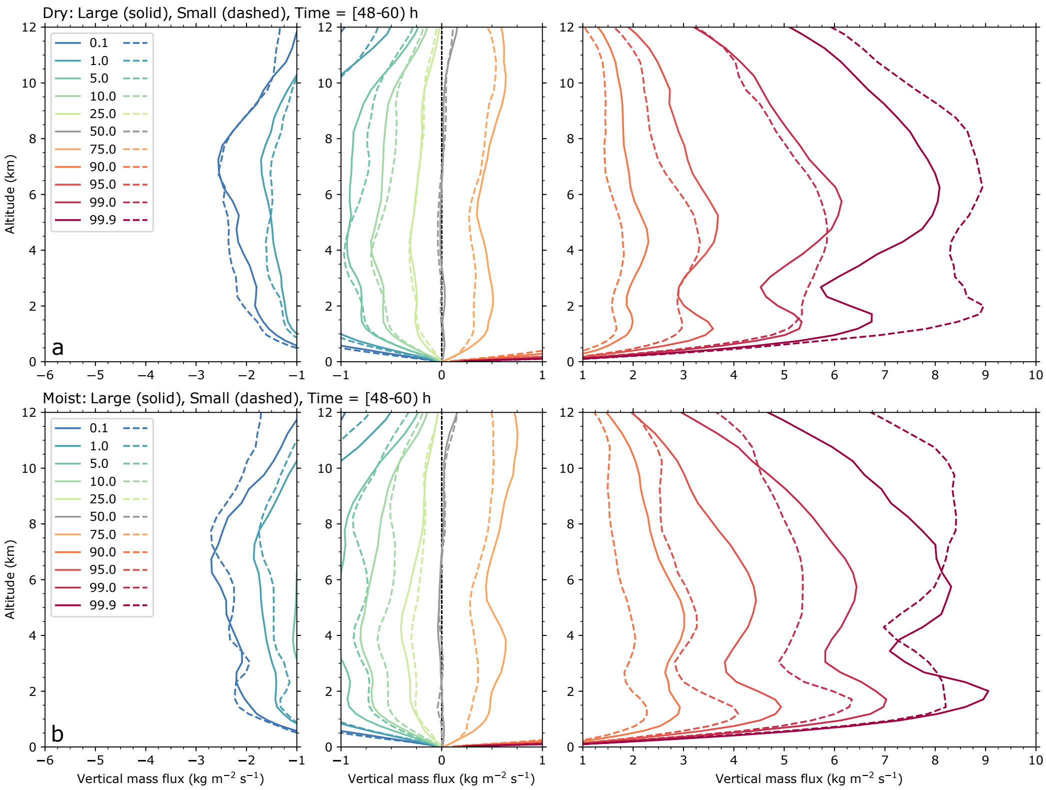

Figure 9. Individual quantiles (colors) from the inner-core ($r \leq 50$ km) vertical mass flux distribution are shown as a function of altitude for each TC between 48–60 h after the initiation of rapid intensification. (a) Vertical mass flux quantiles are shown for the (solid) large, dry (LD) TC and the (dashed) small, dry (SD) TC. (b) Vertical mass flux quantiles are shown for the (solid) large, moist (LM) TC and the (dashed) small, moist (SM) TC. The middle panel is horizontally stretched to twice the spacing between vertical mass flux values compared to the left and right panels.

Figure 9 shows individual quantiles from the inner-core ($r \leq 50$ km) vertical mass flux distribution for each TC between 48–60 h after the initiation of RI. Vertical mass flux quantiles are shown separately for TCs in the dry and moist environments to facilitate comparisons between the small and large TCs. Beginning with the dry environment (Fig. 9a), the LD TC is characterized by a higher frequency of modest-to-large inner-core updraft mass flux throughout 12-km altitude compared to the SD TC; however, the SD TC has a higher frequency of the largest inner-core updraft mass flux values. This result is illustrated by the 75%, 90%, 95%, and 99% updraft mass flux quantiles occurring at larger values for the LD TC, but the 99.9% updraft mass flux quantile occurring at larger values for the SD TC. Furthermore, the LD TC is characterized by a higher frequency of modest-to-large inner-core downdraft mass flux between ~4–10 km altitude compared to the SD TC, but the SD TC has a higher frequency of the largest inner-core downdraft mass flux values.

Transitioning to the moist environment (Fig. 9b), note that differences between the LM and SM TCs are largely similar to those found in the dry environment. One noticeable difference is that a higher frequency of the largest updraft mass flux values for the SM TC is only found above 8-km altitude rather than throughout 12-km altitude as in the dry environment. It is also worth noting that differences in the inner-core vertical mass flux distributions between the small and large TCs are more pronounced in the moist environment compared to the dry environment. In general, the vertical mass flux distributions shown in Fig. 9 demonstrate that subsequent to the bulk intensification phase, an initially large vortex is characterized by a higher frequency of modest-to-large inner-core vertical mass fluxes compared to its relatively smaller counterpart that is instead characterized by a higher frequency of the largest inner-core vertical mass fluxes.

Figure 10 shows individual quantiles from the outer-core ($100 \leq r \leq 300$ km) vertical mass flux distribution for each TC between 48–60 h after the initiation of rapid intensification. The general results are consistent when comparing the small and large TCs for both the dry and moist environments; the large TCs are characterized by larger outer-core updraft and downdraft mass fluxes compared to the small TCs. In contrast to the inner-core vertical mass flux analysis, large TCs exhibit a higher frequency of outer-core updraft and downdraft mass fluxes for all quantiles. A higher frequency of larger outer-core updraft and downdraft mass fluxes for all quantiles corresponds with the greater amount of outer-core convection previously noted for large TCs (see Figs. 6 and 7). Additionally, larger magnitudes of vertical mass flux correspond to relatively stronger outer-

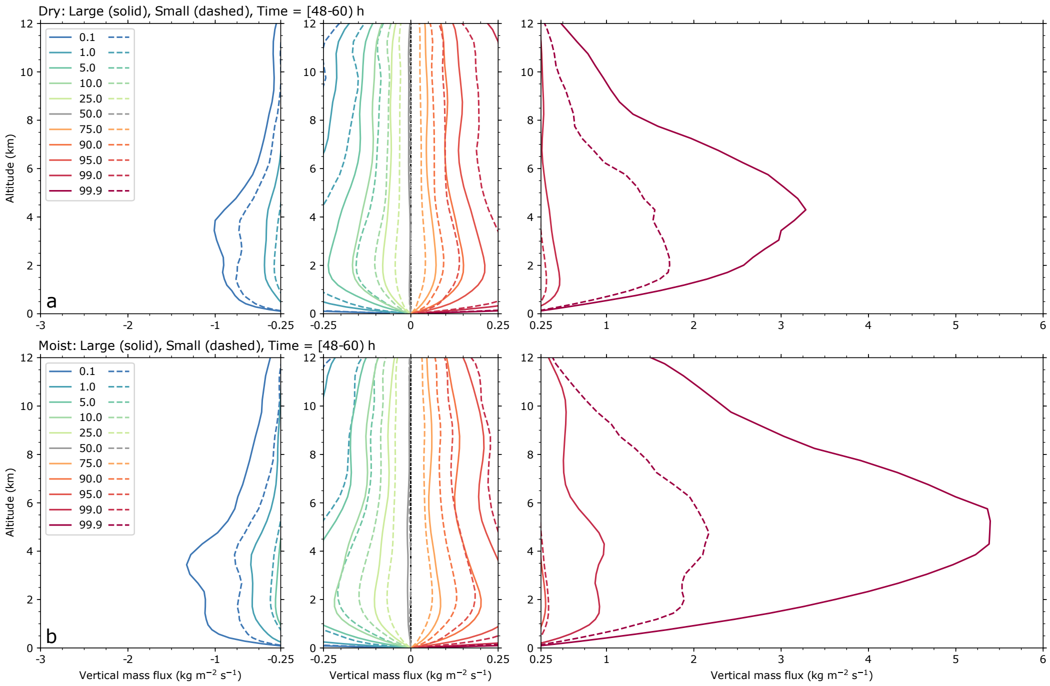

Figure 10. As in Fig. 9, but for the outer-core ($100 \leq r \leq 300$ km) vertical mass flux distribution. The middle panel is horizontally stretched to four times the spacing between vertical mass flux values compared to the left and right panels.

core convection for the large TCs. Collectively, Fig. 10 demonstrates that for a given environment, the large TCs are distinguished from their relatively smaller counterparts by a greater amount of stronger outer-core convection.

3.5 Absolute Circulation Evolution

Results discussed up to this point have demonstrated that large TCs are primarily distinguished from their relatively smaller counterparts by more abundant outer-core convection that occurs at a larger scale and transports a greater amount of mass throughout the troposphere. Here we investigate the relationship between the characteristics of outer-core convection and TC expansion rates via the absolute circulation equation. Following the discussion in section 2 of Davis and Galarneau (2009) and section 1 of Raymond et al. (2011), we formulate the absolute circulation equation in a geometric cylindrical coordinate framework as

$$\frac{\partial C}{\partial t} = -\overline{\eta}_z \widetilde{\delta} A - \oint \eta_z' \mathbf{V}_h' \cdot \hat{\mathbf{n}} dl + \oint w \eta_h \cdot \hat{\mathbf{n}} dl - \oint (\hat{\mathbf{k}} \times \mathbf{F}) \cdot \hat{\mathbf{n}} dl, \tag{8}$$

where C is the absolute circulation, t the time, η_z the absolute vertical vorticity, $\widetilde{\delta}$ the area-averaged horizontal divergence within the area (A) bounded by the integration circuit, $\mathbf{V}_h$ the horizontal velocity vector comprising the radial (u) and tangential (v) velocity components, w the vertical velocity, η_h the horizontal vorticity vector, and $\mathbf{F}$ the three-dimensional friction force vector. In a geometric cylindrical coordinate framework, the integration of terms on the right hand side of Eq. (8) occurs along a circuit of constant radius and altitude, where $\hat{\mathbf{n}}$ is the unit vector that lies in the horizontal plane normal to the circuit, $\hat{\mathbf{k}}$ the vertical unit vector, and dl the incremental length along the circuit path. An overbar denotes the azimuthal mean (i.e., average along the circuit) and primes denote deviations from the azimuthal mean (i.e., asymmetries or eddies). Eq. (8) can be further simplified by noting that in a geometric cylindrical coordinate framework, the radial vector is parallel to the unit normal vector and the azimuthal vector is parallel to the direction of integration along the circuit path (i.e., counter-clockwise). Therefore, Eq. (8) becomes

$$\frac{\partial C}{\partial t} = -\overline{\eta}_z \widetilde{\delta} A - \oint \eta_z' u' dl - \oint w \frac{\partial v}{\partial z} dl + \oint F_t dl, \tag{9}$$

where F_t denotes friction opposing the tangential circulation (i.e., flow along the circuit).

The terms on the right hand side of Eq. (9) represent contributions from 1) the product of area-integrated horizontal divergence within the circuit and azimuthal-mean absolute vorticity along the circuit, 2) asymmetric fluxes of absolute vertical vorticity across the circuit, 3) the flux of absolute vertical vorticity across the circuit arising from tilting horizontal vorticity normal to the circuit, and 4) the flux of absolute vertical vorticity across the circuit associated with friction that opposes the tangential circulation. For simplicity, we henceforth refer to the contributions as stretching, eddy fluxes, tilting, and friction, respectively. Similar to Rios-Berrios et al. (2016), Eq. (9) is normalized by the area of the circuit and integrated forward in time from t_0 to t_1, yielding the area-averaged absolute vorticity change (henceforth, area-averaged vorticity change for simplicity)

$$\begin{aligned} \widetilde{\eta}_z(t_1) - \widetilde{\eta}_z(t_0) \quad = \quad & -\int_{t_0}^{t_1} \overline{\eta}_z \widetilde{\delta} dt - \frac{1}{A} \int_{t_0}^{t_1} \oint \eta_z' u' dl dt \\ & -\frac{1}{A} \int_{t_0}^{t_1} \oint w \frac{\partial v}{\partial z} dl dt + \frac{1}{A} \int_{t_0}^{t_1} \oint F_t dl dt. \end{aligned} \tag{10}$$

We create an ensemble-average analysis centered on the 300-km radius circuit to assess contributions from both the inner- and outer-core convection to the area-averaged vorticity change. The ensemble-average approach is designed to mitigate biases introduced from convective activity concentrated along the circuit (Davis & Galarneau, 2009; Rios-Berrios et al., 2016). To produce an ensemble of circuits, we perturb the radial extent of the circular integration domain ± 12.5 km. Terms on the right hand side of Eq. (10) are then evaluated along each of the circuits and the ensemble average is defined by the area-weighted contributions from all of the circuits.

We note that the area-averaged vorticity change comprises contributions from vortex intensification, strengthening, and expansion (e.g., Merrill, 1984). In particular, the stretching contributions to the area-averaged vorticity change vary as the product between the area-integrated horizontal divergence within the circuit and the azimuthal-mean absolute vertical vorticity along the circuit. We can infer that variations to the horizontal divergence located near the eyewall will impart variations to the stretching contribution evaluated along the 300-km radius circuit; however, we cannot distinguish the "amount" of stretching contributing to vortex intensification and strengthening from the "amount" of stretching contributing to vortex expansion. Therefore, we choose to analyze the area-averaged vorticity change integrated for the 48-h time window beginning 48 h after the initiation of RI. The bulk intensification has completed for each TC 48 h after the initiation of RI (Fig. 3) such that the area-averaged vorticity change is primarily comprised of contributions associated with vortex strengthening and expansion. Additionally, the 48-h integration time window captures the evolution of each TC during the time periods shown in the reflectivity spectral analysis (Fig. 8) and the vertical mass flux analyses (Figs. 9, 10).

Ensemble-averaged terms on the right hand side of Eq. (10) are integrated for the 48-h time window using hourly model output. The sum of terms on the right hand side of Eq. (10) is compared to the net area-averaged vorticity change over the 48-h integration time window on the left hand side. We note that hourly model output reasonably captures the quantitative area-averaged vorticity change for each TC (Fig. 11), providing confidence in the assessment of individual terms in the budget and comparisons between the TCs. We examined all 48-h integration time windows beginning 24-h after the initiation of RI and found that the principal results remain largely consistent (not shown). Toward the later integration time windows for the LM TC (e.g., beginning 72-h after the initiation of RI), the magnitude of stretching begins to decrease rapidly as the TC stops expanding (see Figs. 4d, 5d). We have not thoroughly examined the processes contributing to the structural evolution of the LM TC during this time period and reserve this investigation for future work.

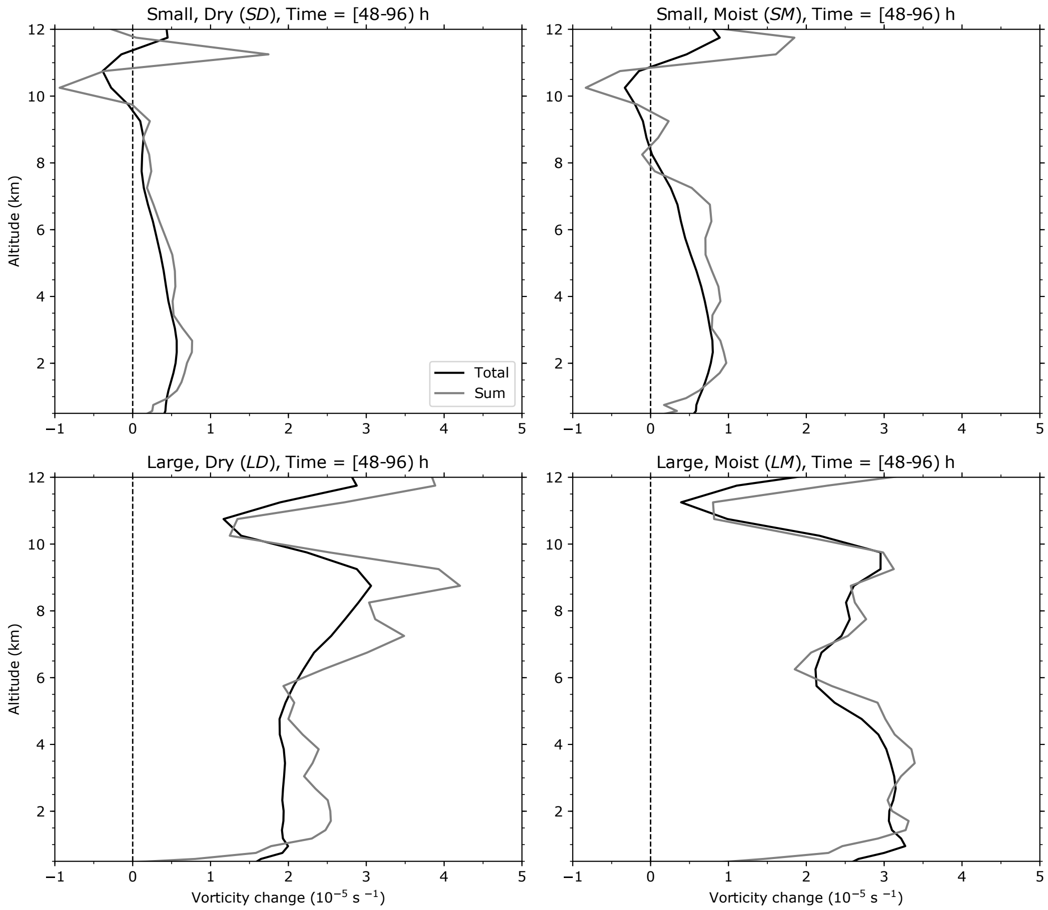

Figure 11. The net area-averaged vorticity change [left hand side of Eq. (10)] over a 48-h time window beginning 48-h after the initiation of RI is shown as a function of altitude for each TC in black. The sum of individual contributions to the net area-averaged vorticity change [right hand side of Eq. (10)] is shown for each respective TC in gray. See text for additional details on the analysis method.

Figure 12 shows the individual contributions on the right hand side of Eq. 10 to the area-averaged vorticity change. In general, as the incipient vortex circulation or environmental moisture increases, the stretching contribution to the net area-averaged vorticity change increases. Contributions from stretching substantiate the statement made earlier that varying the environmental moisture has a larger influence on expansion rates for the large TCs. When comparing the small TCs, increasing the environmental moisture produces a slight increase in the stretching contributions throughout 9-km altitude. In contrast, when comparing the large TCs, increasing the environmental moisture results in approximately twice the stretching contributions throughout 9-km altitude. For a given environmental moisture, the large TCs are characterized by a relative abundance of outer-core convection that occurs at a larger scale compared to their relatively smaller counterparts (see Figs. 7 and 8), resulting in approximately 2–4 times more stretching throughout 9-km altitude.

As the incipient vortex circulation increases, the tilting contribution to the net area-averaged vorticity change also increases. Differences in tilting primarily arise from differences in the amount of convection located near the 300-km radius circuit; large TCs have a greater amount of outer-core convection and therefore larger tilting contributions to the net area-averaged vorticity change. Differences in tilting are smaller between TCs in the moist environment compared to TCs in the dry environment. When comparing the SM and LM TCs, the SM TC is characterized by less outer-core convection compared to the LM TC, but differences in the amount of convection are not as large compared to those between the SD and LD TCs (see Fig. 7). Additionally, differences in the scale of outer-core convection between the SM and LM TCs are smaller than those between the SD and LD TCs (Fig. 8). Therefore, the tilting contribution is approximately 2–3 times larger for the LM TC compared to the SM TC, and approximately 2–4 times larger for the LD TC compared to the SD TC. The differences in tilting contributions to the net area-averaged vorticity change between the large and small TCs generally increases with altitude. Fig. 10 demonstrates that the large TCs have a greater amount of outer-core updraft mass flux at all vertical levels throughout 12-km altitude compared to the small TCs. Given that the large TCs are characterized by an initially larger amount of horizontal vorticity compared to the small TCs, a combination of more upper-level updraft mass flux that tilts stronger horizontal vorticity into the vertical results in a larger upper-level tilting contribution.

In general, the eddy vorticity fluxes provide a negative contribution to the net area-averaged vorticity change throughout a deep layer of the troposphere. Negative contributions from eddy vorticity fluxes indicate that cyclonic vorticity produced by outer-core convection is exported across the circuit, or equivalently, that anticyclonic vorticity is imported across the circuit. Differences in the eddy vorticity fluxes between TCs are relatively small below $\sim$4-km altitude and primarily increase with increasing incipient vortex circulation above 4-km altitude, with large TCs exhibiting a greater (negative) eddy vorticity flux compared to the small TCs. Similar to the differences noted in the tilting contributions between the large and small TCs, a greater amount of upper-level updraft mass flux for the large TCs produces a greater amount of vorticity that can be transported across the circuit; hence, the differences in eddy vorticity flux contributions between the large and small TCs increase with altitude. Finally, larger TCs are characterized by a stronger outer-core tangential circulation compared to the small TCs, and therefore possess a slightly greater (negative) contribution from the friction term in the boundary layer.

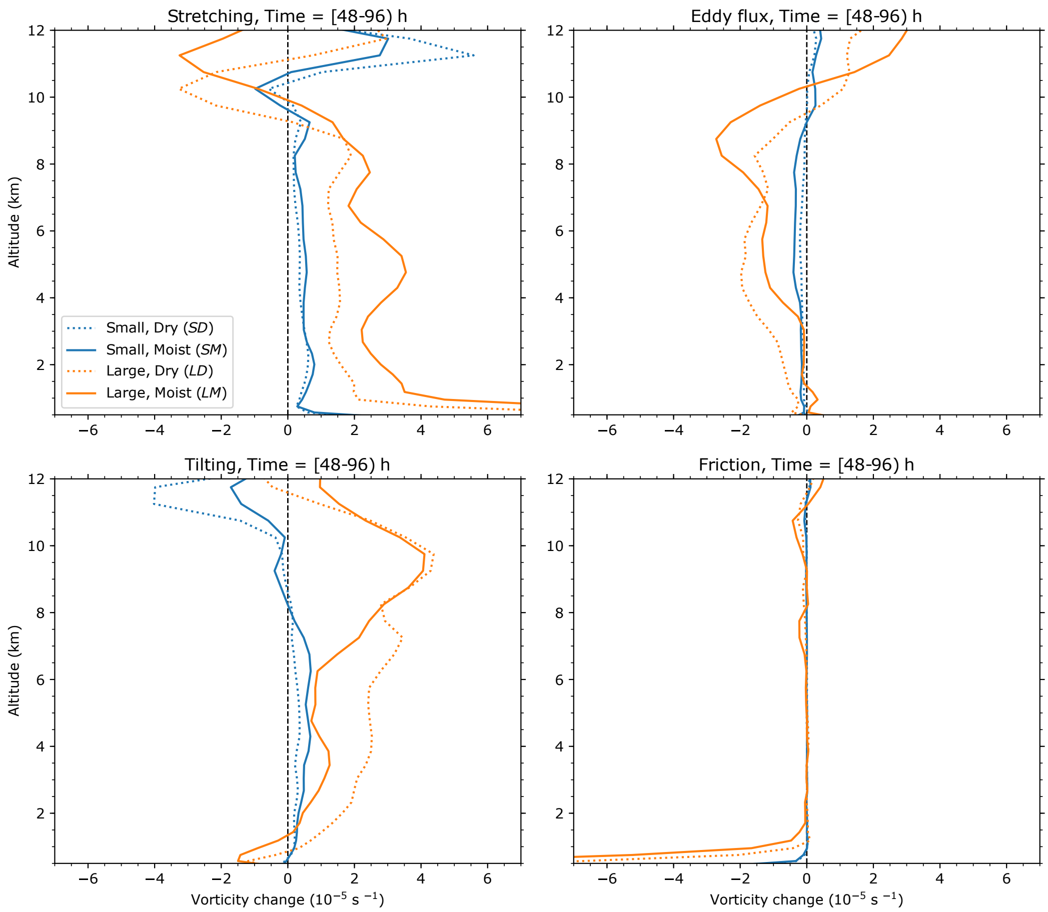

Figure 12. Individual contributions to the area-averaged vorticity change [right hand side of Eq. (10)] are shown as a function of altitude for each TC, distinguished by incipient vortex circulation (color) and mid-level environmental humidity (line style). See text for additional details on the analysis method.

4 Discussion and Conclusions

We have investigated the contributions of incipient vortex circulation and environmental moisture to tropical cyclone (TC) expansion with a set of idealized numerical simulations. The incipient vortex circulation strength is varied by fixing the radius of maximum tangential winds (RMW) and modifying the decay of tangential velocity radially outward of the RMW in accordance with observations of North Atlantic basin TCs (Mallen et al., 2005). The environmental moisture is varied by imposing a vertical decay function that largely preserves moisture content within the boundary layer (below ∼850 hPa) and maximizes the mid-level moisture variance, in accordance with climatological observations of tropical environments (Holloway & Neelin, 2009; Dunion, 2011) and observations of tropical wave disturbances preceding cyclogenesis (Komaromi, 2013; Davis & Ahijevych, 2013).

As discussed in section 1, several past studies have employed similar idealized numerical simulation frameworks to investigate the processes contributing to TC expansion. Hill and Lackmann (2009) posited two potential feedback mechanisms associated with increasing the environmental moisture and producing larger TC expansion rates. Their second feedback mechanism is pertinent to the discussion of results presented herein and we recapitulate the mechanism below. Increasing the environmental moisture of TCs promotes a greater amount of PV generated by radially outward propagating spiral rainbands. PV generated by the spiral rainbands is subsumed by the inner-core PV tower, resulting in a broader PV distribution, and the cyclonic wind field expands in balance with the broader inner-core PV tower. As the cyclonic wind field expands, subsequent heating in spiral rainbands will generate a larger amount of PV given that the diabatic PV tendency is proportional to the magnitude of the absolute vorticity vector. Therefore, an expanding cyclonic wind field promotes a larger amount of PV generation via outward propagating spiral rainbands, which in turn promote an expanding cyclonic wind field; hence, a positive feedback emerges. Although Hill and Lackmann posited this feedback mechanism in association with increasing the environmental moisture, the fundamental processes underlying its premise appear in previous studies that vary the incipient vortex circulation while fixing the environmental moisture (Xu & Wang, 2010; Chan & Chan, 2015; Kilroy & Smith, 2017). Each of these studies emphasize to a varying degree the relationship between the areal distribution of diabatic heating and the magnitude of the absolute vorticity vector and hence their combined influence on TC expansion rates. The findings reported herein are predicated on the same fundamental processes, and thus to a large extent are congruous with the aforementioned studies.

In addition to reproducing findings reported in the aforementioned studies with an independent modeling framework, we further demonstrate that varying the incipient vortex circulation is associated with a scale-dependent response of outer-core convection. Specifically, as the incipient vortex circulation increases, the scale of outer-core convection increases. Increasing the environmental moisture produces a greater amount of outer-core convection, but appears to have a relatively minor influence on its scale in our idealized modeling setup. Therefore, the principal findings reported in this study are primarily attributed to the scale-dependent response of outer-core convection to varying the incipient vortex circulation. Large TCs are distinguished from their relatively smaller counterparts by a relative abundance of outer-core convection occurring at a larger scale that cumulatively spins up the outer-core TC circulation at a quicker rate via combined stretching and tilting; therefore, with all other factors contributing to expansion held constant, the contrast in size between the two TCs will *increase* with time.

Increasing the environmental moisture further promotes convection, thereby modulating the expansion rate; however, in the absence of additional factors contributing to expansion other than incipient vortex circulation, varying the environmental moisture mostly acts to delay or expedite the intensification process. Increasing the environmental moisture for small TCs produces more outer-core convection that occurs at a slightly larger scale, but the overall nature of outer-core convection remains best characterized by isolated convective elements. Therefore, increasing the environmental moisture for small TCs produces a negligible contribution to their expansion rates. On the contrary, increasing the environmental moisture for large TCs produces more outer-core convection at a slightly larger scale. In both moist and dry environments, the nature of outer-core convection for the large TCs is best characterized by spiral rainbands and mesoscale convective systems; however, the large TC in the moist environment benefits from a greater amount of large-scale outer-core convection. Therefore, increasing the environmental moisture for large TCs produces a relatively larger contribution to their expansion rates compared to the small TCs. Together, increasing both the incipient vortex circulation and environmental moisture produces a nonlinear increase in TC expansion rates.

(Schenkel, Lin, Chavas, Vecchi, Oppenheimer, & Brammer, 2018) demonstrated that TCs in the western North Pacific basin experience larger expansion rates compared to TCs in the North Atlantic basin (their Fig. 6). Given that TCs developing in the western North Pacific are on average larger than their North Atlantic counterparts, we hypothesize that the results presented by Schenkel, Lin, Chavas, Vecchi, Oppenheimer, and Brammer (2018) provide evidence to support the principal finding that an initially larger vortex can expand more quickly than its relatively smaller counterpart; however, western North Pacific TCs also develop in environments characterized by larger moisture content and higher sea-surface temperatures compared to North Atlantic hurricanes (e.g., Gray, 1968; Dai, 2006), obscuring statements regarding a direct connection or attribution of either variable in isolation. Additionally, the incipient vortex circulation and environmental moisture are interdependent in nature, further obscuring statements regarding the contributions of either variable in isolation. Therefore, the extent to which the principal finding is manifested within the results presented by Schenkel, Lin, Chavas, Vecchi, Oppenheimer, and Brammer (2018) cannot be estimated, but the parallel between our two studies warrants further investigation.

Previous studies have demonstrated that TCs possess a sort of "memory" with respect to their incipient circulation (Rotunno & Emanuel, 1987; Knaff et al., 2014), which underlies the statement that large TCs stay large and small TCs stay small. Synthesizing the results presented herein, we further demonstrated that a cumulatively larger convergence of angular momentum over time permits an initially large vortex to expand more quickly than its relatively smaller counterpart. Therefore, memory of the incipient vortex circulation is imparted upon TC size through variable expansion rates. Schenkel, Lin, Chavas, Vecchi, Oppenheimer, and Brammer (2018) demonstrate that this memory is largely preserved prior to TCs attaining their lifetime maximum size, but it is attenuated afterwards as TCs begin contracting. Therefore, the principal findings reported herein may only be valid prior to TCs attaining their lifetime maximum size.

There may be several processes contributing to noted differences in the scale of outer-core convection that warrant further investigation. For example, how do variations to the incipient vortex circulation and environmental moisture have an influence on the upscale growth of outer-core convection? Furthermore, we have not examined the duration of outer-core convection given difficulties arising from tracking individual convective elements with hourly model output. We surmise that the scale and duration of outer-core convection are interdependent; thus, their combined influence may in part account for the variable expansion rates noted herein. That is, we expect relatively large-scale convection with a long duration to have a stronger influence on the net area-averaged vorticity change, and hence expansion rate, compared to relatively small-scale convection with a short duration. Additional work is required to elucidate potential relationships between the duration of convection and TC expansion.

Our idealized numerical simulations contain simplifying assumptions that may limit the extent to which our results are found in nature. For example, we begin with an axisymmetric incipient vortex circulation and horizontally homogeneous environmental conditions, but precursor disturbances are intrinsically asymmetric and embedded within spatially inhomogeneous environments (e.g., McTaggart-Cowan et al., 2008, 2013; Chang et al., 2017). Our analysis is limited by excluding contributions from cloud-radiative forcing which have been shown to aid the expansion of TC wind fields by producing weak, sustained ascent in the outer-core region that promotes and enhances convective activity (Bu et al., 2014; Fovell et al., 2016). Furthermore, our analysis is limited by imposing a uniform flow throughout the simulation domain instead of introducing vertical shear flow. Previous studies have demonstrated that a low-level flow vector oriented along the upshear-right quadrant of a TC embedded in vertical shear flow favors larger expansion rates (Chen et al., 2018, 2019). Future work will expand upon the results presented in our study by incorporating the aforementioned considerations into experiments with additional numerical simulations and by comparing the idealized numerical simulations to analyses that combine reanalysis products and satellite observations.

Results gathered from our study can aid the development of statistical–dynamical wind radii forecasts (e.g., Knaff et al., 2017). Furthermore, our results may have implications for understanding how the TC size distribution might shift amidst Earth's warming climate system. Dynamical downscaling projections of TC activity have demonstrated that TC size distributions will shift toward larger TCs in a future, warmer climate among all ocean basins except the western North Pacific (Knutson et al., 2015). Schenkel, Lin, Chavas, Vecchi, Knutson, and Oppenheimer (2018) found that the global TC size distribution will shift toward larger TCs in a future, warmer climate, but that TC size at the time of genesis remains unchanged. Our study motivates additional investigations into how the wind structure of precursor disturbances might vary in a future, warmer climate and associated implications for TC expansion rates among individual ocean basins.

Acknowledgments

This work was funded by the Office of Naval Research awards N000141613033 and N000142012069 and the National Science Foundation (NSF) Award AGS-1701225. JM was also supported by the NSF Bridge to the Doctorate Fellowship Award 004863-00003. We thank George Bryan for providing the code to implement time varying point downscaling in CM1. The model namelists and environmental soundings required to reproduce the simulations analyzed herein can be accessed via the Zenodo repository located at https://zenodo.org/record/3891990.

References

Arakawa, H. (1952). Mame-Taifu or midget typhoon (small storms of typhoon intensity). *Geophys. Mag.*, *24*, 463–474.

Brand, S. (1972). Very large and very small typhoons of the western North Pacific Ocean. *J. Meteor. Soc. Japan*, *50*, 332–341.

Bryan, G. H., & Fritsch, J. M. (2002). A benchmark simulation for moist nonhydrostatic numerical models. *Mon. Wea. Rev.*, *130*, 2917–2928. doi: 10.1175/1520-0493(2002)130⟨2917:ABSFMN⟩2.0.CO;2

Bryan, G. H., & Morrison, H. (2012). Sensitivity of a simulated squall line to horizontal resolution and parameterization of microphysics. *Mon. Wea. Rev.*, *140*, 202-225. doi: 10.1175/MWR-D-11-00046.1

Bryan, H. G., Worsnop, R. P., Lundquist, J. K., & Zhang, J. A. (2017). A simple method for simulating wind profiles in the boundary layer of tropical cyclones. *Bound.-Layer Meteor*, *162*, 475–502. doi: 10.1007/s10546-016-0207-0

Bu, Y. P., Fovell, R. G., & Corbosiero, K. L. (2014). Influence of cloud–radiative forcing on tropical cyclone structure. *J. Atmos. Sci.*, *71*, 1644–1662. doi: 10.1175/JAS-D-13-0265.1

Carrasco, C. A., Landsea, C. W., & Lin, Y.-H. (2014). The influence of tropical cyclone size on its intensification. *Wea. Forecasting*, *29*, 582–590. doi: 10.1175/WAF-D-13-00092.1

Chan, K. T. F., & Chan, J. C. L. (2012). Size and strength of tropical cyclones as inferred from QuikSCAT data. *Mon. Wea. Rev.*, *140*, 811–824. doi: 10.1175/MWR-D-10-05062.1

Chan, K. T. F., & Chan, J. C. L. (2014). Impacts of initial vortex size and planetary vorticity on tropical cyclone size. *Quart. J. Roy. Meteor. Soc.*, *140*, 2235–2248.

doi: 10.1002/qj.2292

Chan, K. T. F., & Chan, J. C. L. (2015). Impacts of vortex intensity and outer winds on tropical cyclone size. *Quart. J. Roy. Meteor. Soc.*, *141*, 525–537. doi: 10.1002/qj.2374

Chang, M., Ho, C.-H., Park, M.-S., Kim, J., & Ahn, M.-H. (2017). Multiday evolution of convective bursts during western North Pacific tropical cyclone development and nondevelopment using geostationary satellite measurements. *J. Geophys. Res. Atmos.*, *122*, 1635–1649. doi: 10.1002/2016JD025535

Chavas, D. R., & Emanuel, K. A. (2010). A QuickSCAT climatology of tropical cyclone size. *Geophys. Res. Lett.*, *37*, L18816. doi: 10.1029/2010GL044558

Chen, B.-F., Davis, C. A., & Kuo, Y.-H. (2018). Effects of low-level flow orientation and vertical shear on the structure and intensity of tropical cyclones. *Mon. Wea. Rev.*, *146*, 2447–2467. doi: 10.1175/MWR-D-17-0379.1

Chen, B.-F., Davis, C. A., & Kuo, Y.-H. (2019). An idealized numerical study of shear-relative low-level mean flow on tropical cyclone intensity and size. *J. Atmos. Sci.*, *76*, 2309–2334. doi: 10.1175/JAS-D-18-0315.1

Czajkowski, J., & Done, J. (2014). As the wind blows? understanding hurricane damages at the local level through a case study analysis. *Weather, Climate, and Society*, *6*(2), 202-217. doi: 10.1175/WCAS-D-13-00024.1

Dai, A. (2006). Recent climatology, variability, and trends in global surface humidity. *J. Climate*, *19*(15), 3589-3606. doi: 10.1175/JCLI3816.1

Davis, C. A., & Ahijevych, D. A. (2013). Thermodynamic environments of deep convection in Atlantic tropical disturbances. *J. Atmos. Sci.*, *70*, 1912–1928. doi: 10.1175/JAS-D-12-0278.1

Davis, C. A., & Galarneau, T. J., Jr. (2009). The vertical structure of mesoscale convective vortices. *J. Atmos. Sci.*, *66*, 686–704. doi: 10.1175/2008JAS2819.1

Doyle, J. D., et al. (2017). A view of tropical cyclones from above: The Tropical Cyclone Intensity (TCI) Experiment. *Bull. Amer. Meteor. Soc.*, *98*, 2113–2134. doi: 10.1175/BAMS-D-16-0055.1

Dunion, J. P. (2011). Rewriting the climatology of the tropical North Atlantic and Caribbean Sea atmosphere. *J. Climate*, *24*, 893–908. doi: 10.1175/2010JCLI3496.1

Dunnavan, G. M., & Diercks, J. W. (1980). An analysis of Super Typhoon Tip (October 1979). *Mon. Wea. Rev.*, *108*, 1915–1923. doi: 10.1175/1520-0493(1980)108⟨1915:AAOSTT⟩2.0.CO;2

Fovell, R. G., Bu, Y. P., Corbosiero, K. L., Tung, W., Cao, Y., Kuo, H., … Su, H. (2016). Influence of cloud microphysics and radiation on tropical cyclone structure and motion. *Meteorological Monographs*, *56*, 11.1–11.27. doi: 10.1175/AMSMONOGRAPHS-D-15-0006.1

Gray, W. H. (1968). Global view of the origin of tropical disturbances and storms. *Mon. Wea. Rev.*, *96*, 669–700.

Harr, P. A., Kalafsky, M. S., & Elsberry, R. L. (1996). Environmental conditions prior to formation of a midget tropical cyclone during TCM-93. *Mon. Wea. Rev.*, *116*, 1693–1710. doi: 10.1175/1520-0493(1996)124⟨1693:ECPTFO⟩2.0.CO;2

Hawkins, H. F., & Imbembo, S. M. (1976). The structure of a small, intense hurricane–Inez 1966. *Mon. Wea. Rev.*, *104*, 418–442. doi: 10.1175/1520-0493(1976)104⟨0418:TSOASI⟩2.0.CO;2

Hawkins, H. F., & Rubsam, D. T. (1966). Hurricane Inez - A classic "micro-hurricane". *Mar. Wea. Log.*, *11*, 157–160.

Hence, D. A., & Houze, R. A., Jr. (2012). Vertical structure of tropical cyclone rainbands as seen by the TRMM precipitation radar. *J. Atmos. Sci.*, *69*, 2644–2661. doi: 10.1175/JAS-D-11-0323.1

Hill, K. A., & Lackmann, G. M. (2009). Influence of environmental humidity on tropical cyclone size. *Mon. Wea. Rev.*, *137*, 3294–3315. doi: 10.1175/2009MWR2679.1

Holloway, C. E., & Neelin, J. D. (2009). Moisture vertical structure, column water vapor, and tropical deep convection. *JAS*, *66*, 1665–1683. doi: 10.1175/2008JAS2806.1

Houze, R. A., Jr. (2010). Clouds in tropical cyclones. *Mon. Wea. Rev.*, *138*, 293–344. doi: 10.1175/2009MWR2989.1

Judt, F., & Chen, S. S. (2016). Predictability and dynamics of tropical cyclone rapid intensification deduced from high-resolution stochastic ensembles. *Mon. Wea. Rev.*, *144*, 4395–4420. doi: 10.1175/MWR-D-15-0413.1

Kaplan, J., DeMaria, M., & Knaff, J. A. (2010). A revised tropical cyclone rapid intensification index for the Atlantic and eastern North Pacific basins. *Wea.*

Forecasting, *25*, 220–241. doi: 10.1175/2009WAF2222280.1

Kepert, J. D. (2012). Choosing a boundary layer parameterization for tropical cyclone modeling. *Mon. Wea. Rev.*, *140*, 1427–1445. doi: 10.1175/MWR-D-11-00217.1

Kilroy, G., & Smith, R. K. (2017). The effects of initial vortex size on tropical cyclogenesis and intensification. *Quart. J. Roy. Meteor. Soc.*. doi: 10.1002/qj.3134

Kimball, S. K., & Mulekar, M. S. (2004). A 15-year climatology of North Atlantic tropical cyclones. Part I: Size parameters. *J. Climate*, *17*, 3555-3575. doi: 10.1175/1520-0442(2004)017⟨3555:AYCONA⟩2.0.CO;2

Klotzbach, P. J., Bell, M. M., Bowen, S. G., & Gibney, E. J. (2020). Surface pressure a more skillful predictor of normalized hurricane damage than maximum sustained wind. *Bull. Amer. Meteor. Soc.*. doi: 10.1175/BAMS-D-19-0062.1

Klotzbach, P. J., Bowen, S. G., Pielke, R. A., Jr., & Bell, M. M. (2018). Continental U.S. hurricane landfall frequency and associated damage: Observations and future risks. *Bull. Amer. Meteor. Soc.*, *99*, 1359–1376. doi: 10.1175/BAMS-D-17-0184.1

Knaff, J. A., Longmore, S. P., & Molenar, D. A. (2014). An objective satellite-based tropical cyclone size climatology. *J. Climate*, *27*, 455–476. doi: 10.1175/JCLI-D-13-00096.1

Knaff, J. A., Sampson, C. R., & Chirokova, G. (2017). A global statistical–dynamical tropical cyclone wind radii forecast scheme. *Wea. Forecasting*, *32*, 629–644. doi: 10.1175/WAF-D-16-0168.1

Knutson, T. R., Sirutis, J. J., Zhao, M., Tuleya, R. E., Bender, M., Vecchi, G. A., ... Chavas, D. (2015). Global projections of intense tropical cyclone activity for the late twenty-first century from dynamical downscaling of CMIP5/RCP4.5 scenarios. *J. Climate*, *28*, 7203–7224. doi: 10.1175/JCLI-D-15-0129.1

Komaromi, W. A. (2013). An investigation of composite dropsonde profiles for developing and nondeveloping tropical waves during the 2010 PREDICT field campaign. *J. Atmos. Sci.*, *70*, 542–558. doi: 10.1175/JAS-D-12-052.1

Liu, K. S., & Chan, J. C. L. (2002). Synoptic flow patterns associated with small and large tropical cyclones over the western North Pacific. *Mon. Wea. Rev.*, *130*, 2134–2142. doi: 10.1175/1520-0493(2002)130⟨2134:SFPAWS⟩2.0.CO;2

Louis, J. F. (1979). A parametric model of vertical eddy fluxes in the atmosphere. *Bound.-Layer Meteor.*, *17*, 187–202. doi: 10.1007/BF00117978

Mallen, K. J., Montgomery, M. T., & Wang, B. (2005). Reexamining the near-core radial structure of the tropical cyclone primary circulation: Implications for vortex resiliency. *J. Atmos. Sci.*, *62*, 408–425. doi: 10.1175/JAS-3377.1

Martinez, J., Bell, M. M., Rogers, R. F., & Doyle, D. J. (2019). Axisymmetric potential vorticity evolution of Hurricane Patricia (2015). *J. Atmos. Sci.*, *76*, 2043–2063. doi: 10.1175/JAS-D-18-0373.1

McTaggart-Cowan, R., Deane, G. D., Bosart, L. F., Davis, C. A., & Galarneau, T. J., Jr. (2008). Climatology of tropical cyclogenesis in the North Atlantic (1948–2004). , *136*, 1284–1304. doi: 10.1175/2007MWR2245.1

McTaggart-Cowan, R., Galarneau, T. J., Bosart, L. F., Moore, R. W., & Martius, O. (2013). A global climatology of baroclinically influenced tropical cyclogenesis. *Monthly Weather Review*, *141*(6), 1963-1989. doi: 10.1175/MWR-D-12-00186.1

Merrill, R. T. (1984). A comparison of large and small tropical cyclones. *Mon. Wea. Rev.*, *112*, 1408–1418. doi: 10.1175/1520-0493(1984)112⟨1408:ACOLAS⟩2.0.CO;2

Musgrave, K. D., Taft, J. L., R. K. Vigh, McNoldy, B. D., & Schubert, W. H. (2012). Time evolution of the intensity and size of tropical cyclones. *J. Adv. Model. Earth Syst.*, *4*, M08001. doi: 10.1029/2011MS000104

Nguyen, L. T., Molinari, J., & Thomas, D. (2014). Evaluation of tropical cyclone center identification methods in numerical models. *Mon. Wea. Rev.*, *142*, 4326–4339. doi: 10.1175/MWR-D-14-00044.1

Nguyen, V. S., Smith, R. K., & Montgomery, M. T. (2008). Tropical-cyclone intensification and predictability in three dimensions. *Quart. J. Roy. Meteor. Soc.*, *134*, 563–582. doi: 10.1002/qj.235

Nolan, D. S. (2007). What is the trigger for tropical cyclogenesis? *Aust. Meteor. Mag.*, *56*, 241–266.

Onderlinde, M. J., & Nolan, D. S. (2017). The tropical cyclone response to changing wind shear using the method of time-varying point-downscaling. *J. Adv. Model. Earth Syst.*, *9*, 908–931. doi: 10.1002/2016MS000796

Raymond, D. J., Sessions, S. L., & Carrillo, C. L. (2011). Thermodynamics of tropical cyclogenesis in the northwest Pacific. *J. Geophys. Res.*, *116*, D18101. doi: 10.1029/2011JD015624

Rios-Berrios, R., Davis, C. A., & Torn, R. D. (2018). A hypothesis for the intensification of tropical cyclones under moderate vertical wind shear. *J. Atmos. Sci.*, *75*, 4149–4173. doi: 10.1175/JAS-D-18-0070.1

Rios-Berrios, R., Torn, R. D., & Davis, C. A. (2016). An ensemble approach to investigate tropical cyclone intensification in sheared environments. Part I: Katia (2011). *J. Atmos. Sci.*, *73*, 71–93. doi: 10.1175/JAS-D-15-0052.1

Rogers, R. F., Aberson, S., Bell, M. M., Cecil, D. J., Doyle, J. D., Kimberlain, T. B., … Velden, C. (2017). Re-writing the tropical record books: The extraordinary intensification of Hurricane Patricia (2015). *Bull. Amer. Meteor. Soc.*. doi: 10.1175/BAMS-D-16-0039.1

Rotunno, R., & Emanuel, K. A. (1987). An air-sea interaction theory for tropical cyclones. Part II: Evolutionary study using a nonhydrostatic axisymmetric numerical model. *J. Atmos. Sci.*, *44*, 542–561. doi: 10.1175/1520-0469(1987)044⟨0542:AAITFT⟩2.0.CO;2

Schenkel, B. A., Lin, N., Chavas, D., Vecchi, G. A., Oppenheimer, M., & Brammer, A. (2018). Lifetime evolution of outer tropical cyclone size and structure as diagnosed from reanalysis and climate model data. *J. Climate*, *31*, 7985–8004. doi: 10.1175/JCLI-D-17-0630.1

Schenkel, B. A., Lin, N., Chavas, D. R., Vecchi, G. A., Knutson, T. R., & Oppenheimer, M. (2018). *Will outer tropical cyclone size change due to anthropogenic warming?* (*33rd Conference on Hurricanes and Tropical Meteorology*, Jacksonville, FL, Amer. Meteor. Soc., https://ams.confex.com/ams/33HURRICANE/webprogram/Paper339539.html)

Tao, D., Bell, M., Rotunno, R., & van Leeuwen, P. J. (2020). Why do the maximum intensities in modeled tropical cyclones vary under the same environmental conditions? *Geophysical Research Letters*, *47*(3), e2019GL085980. doi: 10.1029/2019GL085980

Tao, D., & Zhang, F. (2014). Effect of environmental shear, sea-surface temperature, and ambient moisture on the formation and predictability of tropical cyclones: An ensemble-mean perspective. *Journal of Advances in Modeling*

Earth Systems, *6*(2), 384-404. doi: 10.1002/2014MS000314

Weatherford, C. L., & Gray, W. M. (1988). Typhoon structure as revealed by aircraft reconnaissance. Part II: Structural variability. *Mon. Wea. Rev.*, *116*, 1044–1056. doi: 10.1175/1520-0493(1988)116⟨1044:TSARBA⟩2.0.CO;2

Xu, J., & Wang, Y. (2010). Sensitivity of the simulated tropical cyclone inner-core size to the initial vortex size. *Mon. Wea. Rev.*, *138*, 4135–4157. doi: 10.1175/2010MWR3335.1

Xu, J., & Wang, Y. (2018). Effect of the initial vortex structure on intensification of a numerically simulated tropical cyclone. *J. Meteor. Soc. Japan*, *96*, 111–126. doi: 10.2151/jmsj.2018-014

Zhai, A. R., & Jiang, H. J. (2014). Dependence of US hurricane economic loss on maximum wind speed and storm size. *Environ. Res. Lett.*, *9*, 064019. doi: 10.1088/1748-9326/9/6/064019